Ionic Transport in Pure and Doped $LiZr_2(PO_4)_3$ Polymorphs

M.Tech. Thesis

By

MILIND KUMAR

DISCIPLINE OF METALLUGY ENGINEERING AND MATERIALS SCIENCE

INDIAN INSTITUTE OF TECHNOLOGY INDORE

JUNE, 2018

Ionic Transport in Pure and Doped $LiZr_2(PO_4)_3$ Polymorphs

A THESIS

Submitted in partial fulfillment of the requirements for the award of the degree

of

Master of Technology

by

MILIND KUMAR

DISCIPLINE OF METALLURGY ENGINEERING AND MATERIALS SCIENCE

INDIAN INSTITUTE OF TECHNOLOGY INDORE

JUNE, 2018

Indian Institute Of Technology Indore

Candidate's Declaration

I hereby certify that the work which is being presented in the thesis entitled **Ionic Transport in Pure and Doped $LiZr_2(PO_4)_3$ Polymorphs** in the partial fulfillment of the requirements for the award of the degree of **MASTER OF TECHNOLOGY** and submitted in the **DISCIPLINE OF Metallurgy Engineering and Materials Science, Indian Institute of Technology Indore**, is an authentic record of my own work carried out during the time period from July 2016 to June 2018 under the supervision of Dr. Sunil Kumar, INSPIRE faculty, Discipline of Metallurgy Engineering and Materials Science and Dr. Parasharam M. Shirage, Associate Professor, Discipline of Metallurgy Engineering and Material Science.

The matter presented in this thesis has not been submitted by me for the award of any other degree of this or any other institute.

Signature of the student with date

This is to certify that the above statement made by the candidate is correct to the best of my/our knowledge.

Signature of the Supervisor
Date:
Dr. Sunil Kumar

Signature of the Supervisor
Date:
Dr. Parasharam M. Shirage

MILIND KUMAR has successfully given his M.Tech. Oral Examination held on

Signature of Supervisor of M.Tech. thesis
Date:

Convener, DPGC
Date:

Signature of PSPC Member #1
Date:

Signature of PSPC Member #2
Date:

ACKNOWLEDGEMENTS

To complete this thesis, it required enormous effort and determination. However, the successful result would not have been achieved if there was no help from very special people.

First of all, I would like to express my gratitude to my supervisor, **Dr. Sunil Kumar**. I am indebted to him for the on-time completion of this thesis.

Secondly, I am sincerely thankful to **Dr. Parasharam M. Shirage** for his constructive directions and supervision. He led me to the right path of research.

Thirdly, I am very grateful to **Prof. Pradeep Mathur, Director, IIT Indore,** for providing the essential facilities, valuable guidance, and cooperation.

I take this opportunity to express my profound gratitude towards my PSPC members, **Dr. Rupesh Devan** and **Dr. Kiran Bala** for their guidance and support. I am also thankful to **Dr. I.A.Palani, HOD, Discipline of MEMS** for his support and cooperation. I am thankful to all the **faculty members** of the MEMS Discipline for their immense guidance and support.

For my group mates, **Arun Kumar Yadav, Saniya Ayaz, Anita Verma, Tanvi Pareek, Sushmita Dwivedi and Rohit R.S.,** thank you guys for the useful discussion and friendship.

Finally, from the bottom of my heart, I would like to express my deepest affection to my mother **Mamta Kumari**, my father **Manoj Kumar** and my grandparents for their endless encouragement and support.

MILIND KUMAR

.....Dedicated to my Mother,

&

.....My Father

Abstract

Safety issue associated with the high flammability and volatility of organic electrolytes used in commercial rechargeable lithium-ion batteries has led to significant attention to ceramic-based solid electrolytes. A detailed study of ion conduction mechanisms in these ceramics is one of the key features for the development of solid electrolytes for application in rechargeable lithium batteries. In this regard, the NaSICON-type framework has been extensively investigated in a bid to design new compounds with improved room temperature lithium ionic conductivity. $LiZr_2(PO_4)_3$ is an important compound in view of the reported high reduction potential against lithium metal which makes it an attractive candidate for use as an electrolyte in high energy density batteries. However, reported ionic conductivity in $LiZr_2(PO_4)_3$ is still lower than what is required for a potential electrolyte in practical battery applications. This thesis, therefore, deals with investigations on the lithium ion conduction in monoclinic and rhombohedral phases of $LiZr_2(PO_4)_3$. Influence of $(SiO_4)^{4-}$ substitution for $(PO_4)^{3-}$ on the structure and physical properties of $LiZr_2(PO_4)_3$ ceramics is studied using some experimental techniques.

Chapter 1 introduces the field of solid-state lithium ion conductors or solid electrolytes (for lithium-ion batteries) as well as their need in the present global scenario. Chapter 2 describes the working principle of a typical lithium-ion battery, classification of different solid electrolytes and fundamentals of ion transport in these solids. The literature on fast ion conducting electrolytes is reviewed. Finally, the objective of the present study is stated.

Chapter 3 describes the various techniques used in this project, which include, both synthesis and characterization techniques. Various experimental techniques such as density measurement, X-ray diffraction, Field Effect Scanning Electron Microscopy and room temperature and high-temperature dielectric measurements are employed to characterize structural, microstructural, and electrical properties of ceramic solid electrolytes.

Results of the present work are presented and discussed in Chapter 4. X-ray diffraction data revealed that the $LiZr_2(PO_4)_3$ crystallized in two polymorphs depending on the calcination temperature and confirmed that $P2_1/n$ and $R\bar{3}c$ are the appropriate space groups for the sample synthesized at 900 ºC and 1300 ºC, respectively. Further, density value has been increased with (a) higher sintering temperature and (b) increase in concentration of Si in the general formula $Li_{1+3x}Zr_2(P_{1-x}Si_xO_4)_3$ for (x = 0, 0.05 and 0.1). FE-SEM result of $LiZr_2(PO_4)_3$ ceramics shows good sintered samples with few micro-cracks due to anisotropic growth of the rhombohedral unit cell. Finally, results of the temperature dependent dielectric measurements were analyzed, and it was found that conductivity of high-temperature phase (Rhombohedral) was two orders higher than the low-temperature phase (Monoclinic). It also shows that activation energy (E_A) value also changes with (a) change in calcination/sintering temperature, (b) concentration of the $(SiO4)^{4-}$ dopant in the $LiZr_2(PO_4)_3$.

The conclusions of the present work are presented in Chapter 5.

LIST OF PUBLICATIONS/ CONFERENCES

1. Milind kumar, Arun Kumar Yadav, Anita, Somaditya Sen and Sunil kumar, "Lithium ion conduction is sol-gel synthesized $LiZr_2(PO_4)_3$ polymorphs" *AIP Conference Proceedings*, vol.1942, article 140026(2018), 2018.

TABLE OF CONTENTS

LIST OF FIGURES

LIST OF TABLES

NOMENCLATURE

RT – Room temperature

HT – High Temperature

DOD – Depth of Discharge

SOC – State of Charge

LZP – Lithium Zirconium Phosphate ($LiZr_2(PO_4)_3$)

LLTO – Lithium Lanthanum Titanate ($Li_{0.21}La_{0.597}TiO_3$)

LLZO- Lithium Lanthanum Zirconate ($Li_7La_3Zr_2O_{12}$)

LZP-M / LZP-00-M – $LiZr_2(PO_4)_3$ sample monoclinic phase

LZP-R / LZP-00-R – $LiZr_2(PO_4)_3$ sample rhombohedral phase

LZPS-05-M – $Li_{1.15}Zr_2(P_{0.95}Si_{0.05}O_4)_3$ sample monoclinic phase

LZPS-05-R – $Li_{1.15}Zr_2(P_{0.95}Si_{0.05}O_4)_3$ sample rhombohedral phase

LZPS-10-M – $Li_{1.3}Zr_2(P_{0.9}Si_{0.1}O_4)_3$ sample monoclinic phase

LZPS-10-R – $Li_{1.3}Zr_2(P_{0.9}Si_{0.1}O_4)_3$ sample rhombohedral phase

CPE – Constant Phase Element

ACRONYMS

FE-SEM – Field Effect Scanning Electron Microscopy

SEI – Solid Electrolyte Interphases

ASLBs – All Solid-State Batteries

LAB – Lithium Air Battery

LIBs – Lithium-ion Batteries

Lipon – Lithium Phosphorous oxynitride ($Li_{2.88}PO_{3.73}N_{0.14}$)

LB – Lithium Batteries

LPB – Lithium Polymer Battery

LM – Lithium Micro-battery

NaSICON – Sodium Super Ionic Conductors

LISICON – Lithium Super Ionic Conductors

SEM – Scanning Electron Microscopy

BSE – Back Scattered Electrons

SE – Secondary Electrons

AC – Alternating Current

EIS – Electrochemical Impedance Spectroscopy

Chapter 1

INTRODUCTION

1.1 INTRODUCTION and MOTIVATION

This thesis focuses on ion-conduction behavior of Lithium Zirconium Phosphate (LZP) solid electrolyte, as well as on the effects of $(SiO_4)^{4-}$ substitution for $(PO_4)^{3-}$ on its structural and electrical properties. Chapter 2 describes various solid electrolytes, and their conductivity behavior. Chapter 3 includes the experimental techniques employed for synthesis, processing, and characterization. Chapter 4 describes the structural and microstructural characterization of the compound LZP and its dopants as well as their impedance behavior. Chapter 5 concludes the important results obtained from the studies carried out as a part of the thesis.

If we pry open one of today's ubiquitous high-tech devices — whether a cellphone, a laptop, or an electric car — we find that batteries take up most of the space inside. Indeed, the recent evolution of batteries due to advancement in the field of nanotechnology has made it possible to pack significantly large power in a small space. Yet, new applications demand batteries to last even longer. Accordingly, tremendous efforts have been made to amplify the power that a given size battery can hold. Lithium batteries with increased energy density are required for the rapidly growing markets such as electric vehicles and grid storage. The high energy density can be obtained by utilizing cathodes with either high capacity or high voltage. While incorporating high capacity cathodes usually requires exploring new compound and phases, high-voltage cathodes can be designed relatively easily by cation substitution in existing compounds, without altering much the crystal structure or the intercalation chemistry [1-4]. Rare, but widely known, incidents of overheating or combustion in lithium-ion batteries have also highlighted the importance of safety in battery technology.

The high-voltage cathodes potentially increase the energy density of lithium batteries by 20-50%, but the commercial use of these batteries are impeded by the

intrinsic problems of the conventional batteries: the narrow electrochemical window of liquid electrolyte, and dissolution of transition metals from the cathode, and poor safety of the liquid electrolyte. The high operating voltages of the aforementioned cathode compounds are surpassing the voltage window of the carbonate-based electrolyte, 4.3 V; thus, the electrolyte undergoes apparently continuous oxidative decomposition during cycling and forms non-passivating solid electrolyte interphases (SEI) films on the cathodes. As a result, low Coloumbic efficiency is usually observed for high-voltages cathode based half-cells (where metallic Li is used as an anode) [5-8] and the cycle life of high-voltage full cells (where the amount of Li ions is limited) is dramatically limited [7, 9]. Also, the non-passivating nature of cathodic SEI film results in chemical etching of the cathodes by electrolytes and the dissolution of transition metal ions [9, 10]. These dissolved transition metals decrease the available capacity in cathodes and increase the thickness of SEI films [9]. Furthermore, safety is a great concern for high-voltage Lithium-ion batteries, where the liquid electrolytes, containing flammable esters and ethers, are intervened beyond their stable voltage limits. Lastly, lithium batteries with Li metal anodes were not commercialized because of the notorious problem associated with Li dendrite growth during lithium cycling [11] and the lithium-ion batteries with graphitic anodes are practically used at the cost of much-lowered capacity and operating voltage. Although tremendous research has been devoted to developing new electrolytes with expanded safety window [6, 12, 13] as well as modifying the surface of anodes [14] and cathodes [5, 10, 15-19] for improved stability, it is not easy to address the above four problems concurrently. High-voltage lithium batteries can be successfully utilized only if all these problems associated with the cathode, the electrolyte, and the anode are solved fully.

In light of the problems discussed above, researchers have developed a new approach to one of the three basic components of batteries, the electrolyte. The new findings are based on the idea that a solid electrolyte, rather than the liquid used in today's most common rechargeable, could significantly improve both device lifetime and safety — while providing a significant boost in the amount of power stored in a given space. It is well-known fact that many solid electrolytes have a voltage window beyond 5 V and thus do not decompose under anodic

currents such as $Li_{10}GeP_2S_{12}$ [20], Li_3PS_4 [14], Li_4SnS_4 [21], $Li_7La_3Zr_2O_{12}$ [22], and Lithium phosphorous oxynitride (Lipon) [23]. Furthermore, with a solid electrolyte, the concern of transition metal dissolution into the electrolyte is minimal. In comparison with carbonate electrolytes, most ceramic electrolytes are intrinsically non-flammable. Lastly, lithium metal is compatible with many solid electrolytes and is less likely to form dendrites during cycling because of the mechanical robustness of the solid electrolyte [24-26]. Few of the major problems associated with solid-state batteries are their low power densities compared with electrolyte lithium batteries, resulting from the low ionic conductivity of the solid electrolyte, the electrode/electrolyte interfacial compatibility and limited kinetics of the electrodes [27, 28]. The recently designed solid electrolytes with high ionic conductivity enable the possibility of fabricating solid-state lithium batteries with a power performance comparable to that of liquid-electrolyte batteries [20, 29]. On the other hand, interfacial instability between the electrode and electrolyte is of great challenge for solid-state batteries [20, 21, 30, 31]. Proper engineering at the interfaces of electrode/electrolyte is the need for good performance of most solid-state lithium batteries [20, 31-33]. Nevertheless, compared with liquid counterparts, solid electrolytes are nonflammable, corrosion resistance, leakage, and evaporation, and exhibit the intrinsic potential to prevent internal cell short circuit caused by the direct contact of active electrode components and the possibility for miniaturization using thin-film processing techniques. Therefore, lithium batteries using solid electrolytes, i.e. all-solid-state batteries (ASLBs), are regarded to be intrinsically safe with largely enhanced cycle life as compared with the commercial ones using organic liquid electrolytes, thus holding high promise to be used in large scale for energy storage in transportation and grid balance (electrical utility load leveling).

To be used as solid electrolytes in lithium-based batteries, especially in the future wide applications for large-scale energy storage, the materials should ideally have high lithium-ion conductivity (e.g. $>10^{-4}$ S/cm) at RT [34], negligible electronic conductivity (i.e. Li^+ ion transference number close to unity), wide electrochemical window (e.g. > 6 V vs Li^+/Li) and stability with respect to adjacent electrodes (cathodes and metallic lithium), stability against heat

treatment and moisture/aqueous solution, suitable mechanical properties, ready availability of chemical constituents, ease of fabrication, and reasonable cost.

Chapter 2

SOLID ELECTROLYTES

2.1 Introduction

Lithium batteries (LB) are among the myriad power sources for the XXI century energy economy. However, these devices are relatively adequate primarily for small applications, and their performances are far from to be satisfactory for automotive applications chiefly in terms of energy densities and power densities, safety and cyclability. This makes them very interesting and attractive from the point of view of basic science [11] and materials development [35, 36].

During the last decade, several LB classification schemes were suggested on the basis of the electrodes and electrolyte nature and design. However, these terms are sometimes confusing, and therefore may be useful to reconsider them in a critical fashion. LB is the common name given to primary (disposable) devices having lithium metal or a lithium compound as the anode. Lithium-ion battery (LIB) includes a family of secondary (rechargeable) devices where both the electrodes are intercalation compounds, and the electrolyte is a lithium salt dissolved in a mixture of organic solvents. Lithium polymer battery (LPB, LIPB) is a rechargeable device where the lithium salt is somehow trapped in a polymer (or composite) membrane. The anode may be Li metal or a Li-based intercalation material, and the cathode is an intercalation oxide. Lithium-air battery (LAB) is a device where a lithium metal anode is electrochemically coupled with the atmosphere through a composite (conducting carbon and catalysts) cathode, the electrolyte being liquid or polymer-based. The main advantage of this device is given by its very high specific energy, 11140 Wh kg^{-1} (theoretical, excluding oxygen), which is not far from that of gasoline/air engine (11860 Wh kg^{-1}). Finally, micro lithium battery (LM) is an all solid-state thin film device, where the anode may be Li metal or an intercalation material, the cathode is an intercalation compound, and the electrolyte is a glassy, glass-ceramic or ceramic Li^+ conductor.

Capacitors and batteries are both used in numerous energy storage applications, but for different purposes. Traditional capacitors store energy through electrostatic charging at their electrode-electrolyte interfaces under an applied potential. This process allows capacitors to deliver energy very rapidly, but only in small amounts. In contrast, batteries store energy through electrochemical reactions that typically occur throughout the entire bulk of their electrode active materials, thereby allowing comparatively large amounts of energy to be stored, although without being as quickly delivered as in capacitors. This power/energy trade-off is captured in so-called Ragone plot, shown in Figure 1.

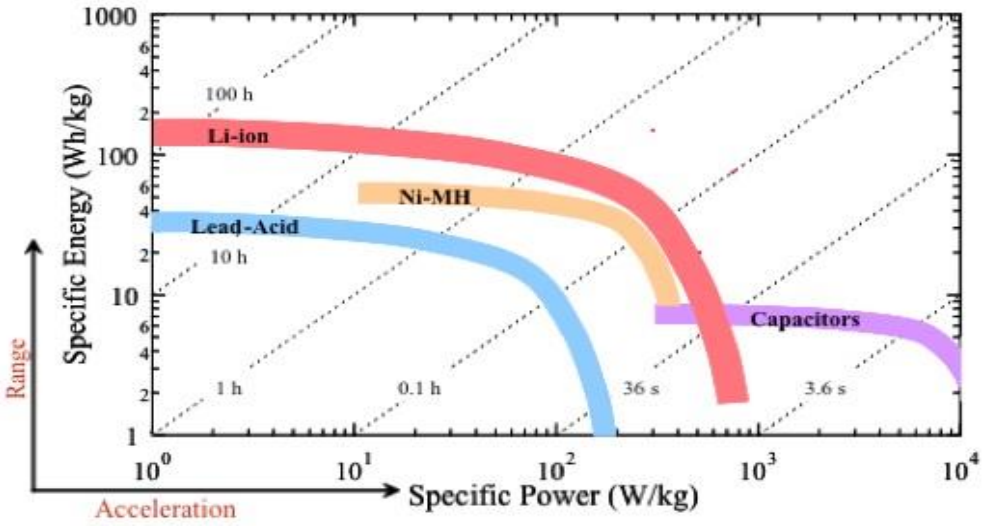

Figure 1: Ragone plot comparing various electrochemical energy storage devices.

Energy storage research generally focuses on moving every device's performance closer to the upper right-hand corner of this plot. For capacitors, increasing specific energy is critical and remains a limitation impending them from being implemented in large-scale energy storage systems. To increase energy density, researchers are actively pursuing new electrolytes that will possibly provide a wide operating potential stability window, as well as understanding how to amplify the charge stored in electrode materials at a given applied electrostatic potential [37-39]. For batteries, many directions are currently being pursued to

impart higher energy storage and lower cost than current state-of-the-art Li-ion batteries.

2.2 WORKING PRINCIPLE OF LITHIUM-ION BATTERIES

A Li-ion battery is built by connecting several basic Li-ion cells in parallel (to increase current), in series (to increase voltage) or combined configurations. Multiple battery cells can be blended into a module. Multiple modules can be integrated into a battery pack. For example, the 85 kWh battery pack in a Tesla car contains 7104 cells (18650-type cells). Typically, a basic Li-ion cell consists of a cathode (positive electrode) and an anode (negative electrode) which are contacted by an electrolyte containing lithium ions. The electrodes are separated from each other by a separator, typically micro-porous polymer membrane, which allows the exchange of lithium ions between the two electrodes. Figure 2 illustrates the basic operating principle of Li-ion battery cell. The basic design of Li-ion cells today is still the same as those cells Sony commercialized two decades ago, although various kinds of electrode materials, electrolytes, and separators have been explored.

The commercial cells are typically assembled in the discharged state. The discharged cathode materials (e.g., $LiCoO_2$, $LiFePO_4$) and anode materials (e.g., graphite) are stable in ambient atmosphere and can be easily handled in industrial practices.

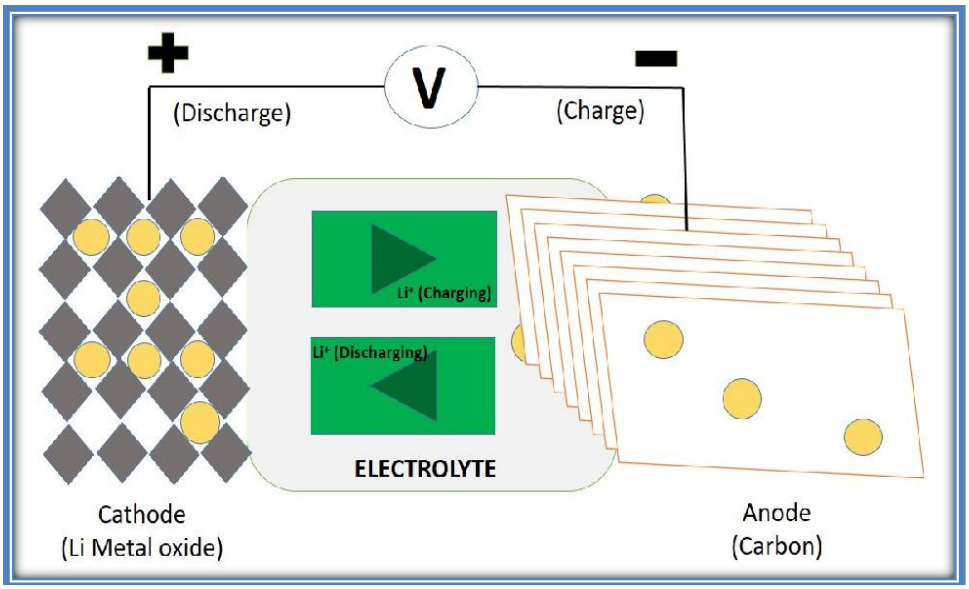

Figure 2: Operating principle of Lithium-ion batteries.

During charging process, the two electrodes are connected externally to an electrical supply. The electrons are forced to be released at the cathode, and move externally to the anode. At the same time, the lithium ions move in the same direction, but internally from cathode to anode, *via* the electrolyte. In this way the electrical energy are electrochemically stored in the battery in the form of chemical energy in the anode and cathode materials with different chemical potentials. The opposite occurs during the discharging process: electrons move from anode to cathode through the external load to do the work and Li-ions move from anode to cathode in the electrolyte. This is known as "shuttle chair" or "rocking chair" mechanism, where Li-ions shuttle between the anode and the cathodes during charging and discharging.

The performance of Li-ion batteries can be assessed by a number of parameters, such as specific energy, volumetric energy, specific capacity, cyclability, safety, abuse tolerance, and dis/charging rate. Specific energy (Wh/kg) quantifies the amount of energy that can be stored and released per unit mass of the battery. It can be calculated by multiplying the specific capacity (Ah/kg) with operating voltage (V). Specific capacity gives the amount of charge that can be reversibly stored per unit mass. It is closely related to the number of electrons released from the electrochemical reactions and the atomic weight of the material.

Cyclability measures the reversibility of the Li-ion insertion and extraction processes, in terms of number of charge and discharge cycles before battery loses energy significantly or can no longer sustain function of the device it powers. Practically, the cycle life of Li-ion batteries is governed by the depth of discharge (DOD) and state of charge (SOC), as well as operating temperature, in addition to the battery chemistry. Cycle life can be magnified with shallow DOD cycles and less SOC swing and avoiding elevated/high operating temperature.

Abuse tolerance is a critical requirement for commercial application of Li-ion batteries, especially in electric vehicles. Usually, mechanical, thermal, and electrical abuse evaluations are carried out on prototypes to evaluate the abuse tolerance of the batteries. The mechanical abuse evaluation incorporates mechanical shock and drop, roll-over, nail penetration, and immersion in water tests. The thermal abuse evaluation includes radiant heat, thermal stability, overheat, and extreme cold tests. The electrical abuse evaluation comprises of a short circuit, overcharge, over-discharge, and alternating current exposure tests. Those abuse tolerance tests are extremely important for their applications in electric vehicles, as electric vehicles are supposed to compete with existing internal combustion -powered vehicles that run well in rough conditions. The rate of charge or discharge measures how fast the battery can be charged or discharged, typically called C-rate. At 1 C, the battery is fully discharged releasing maximum capacity in 1 hour. Table 1 depicts the comparison of such specifications of various rechargeable batteries.

Specifications	Lead Acid	NiCd	NiMH	Li-ion
Specific Energy (Wh/kg.)	30-50	45-80	60-120	150-250
Cycle Life (80% DOD)	200-300	1000	300-500	500-1000
Charge Time	8-16h	1-2h	2-4h	2-4h
Overcharge Tolerance	High	Moderate	Low	Low
Self Discharge/month (RT)	5%	20%	30%	<5%
Cell voltage	2V	1.2V	1.2V	3.6V
Cost	Low	Moderate	Moderate	High

Table 1: Comparison of various rechargeable batteries.

A modern-day commercial lithium-ion battery typically uses 1 M solution of $LiPF_6$ in EC-DMC (ethylene carbonate and dimethyl carbonate in 1:1 volume ratio). Major drawbacks associated with such organic liquid electrolytes are:

- Narrow electrochemical window (4.3 V typically).
- Dissolution of transition metals from the cathode.
- Flammable
- Notorious problem of dendrite growth.

Replacing the electrolytic solution in the lithium-ion battery with a solid electrolyte has the following advantages:-

- Greater safety because there are no combustible organic liquids.
- Higher energy density enabled by integration with high voltage, high capacity electrodes in dense packing.
- A wide range of compatible electrode materials Minimal self-discharge.
- Wider operating temperature window.

Ideally, a solid-state lithium ionic conductor should meet the following requirements for it to be used as a solid electrolyte in battery applications:-

- High lithium ionic conductivity at operating temperature; RT is preferred.
- Negligible electronic conductivity.
- Low grain boundary resistance.

- Chemical and electrochemical stability against reactions with electrodes, such as Li metal.
- Low interfacial resistances with both the electrode materials.

These criteria turn out to be difficult to meet for most available materials. Many known materials have either high ionic conductivity or good chemical stability but not both. Some of the materials which are found to have potential as solid electrolytes are discussed in the following section.

2.3 LITERATURE REVIEW

Solid electrolyte is the critical component in a solid-state battery. It can also be used with liquid electrolyte in other configurations, such as a flow battery system, organic-aqueous hybrid electrolyte lithium-air battery, etc. Solid electrolyte can be loosely categorized into three types: inorganic solid electrolytes, organic solid electrolytes, and organic composite solid electrolytes. The organic and organic composite electrolytes generally consist of a polymer, lithium salts and, optionally solid fillers. A brief discussion on the inorganic solid electrolytes is provided in the section below.

2.3.1 Solid electrolytes with Perovskite structure.

The perovskite structured lithium lanthanum titanate ($Li_{1-3x}La_xTiO_3$ in LLTO) has one of the highest RT lithium ionic conductivity (10^{-3} S cm^{-1}) among solid inorganic electrolytes. Conduction of lithium ions in LLTO is through the A-site vacancies, and the size of the bottleneck between A sites determines the activation energy (Figure 3). Thus, the lithium concentration is critical to the ionic conductivity. The highest bulk ionic conductivity of 10^{-3} S cm^{-1} at RT is exhibited by the composition with x = 0.11 [40] and it is attributed to the optimum concentration of lithium ions and available vacancies for lithium-ion hopping. It is further shown that the cubic structured LLTO shows somewhat higher lithium

ionic conductivity than the tetragonal polymorphs [41]. Some of the known issues associated with the LLTO are:

a) Densification of LLTO requires a high sintering temperature which definitely leads to loss of lithium [42]. So, controlling the exact stoichiometry and chemical homogeneity is rather difficult. As the Li^+ conductivity is highly dependent on the number of the available A-site vacancies, any variation from the intended stoichiometry severely degrades the conductivity.
b) High grain boundary resistance is another problem associated with polycrystalline LLTO has a total ionic conductivity of 10^{-5} S cm^{-1} at RT which is two orders of magnitude lower than the bulk conductivity, due to chemical and structural deviations and impurity formation at the grain boundaries [43, 44].
c) Reduction of Ti^{4+} in contact with metallic Li anode is another problematic issue which necessities the fabrication of so-called protected lithium electrode where a protective film is deposited on the lithium to protect it from the direct contact with solid electrolytes. Reduction of Ti^{4+} results in an increase in the electronic conductivity, which is undesirable for solid electrolytes in lithium metal batteries.

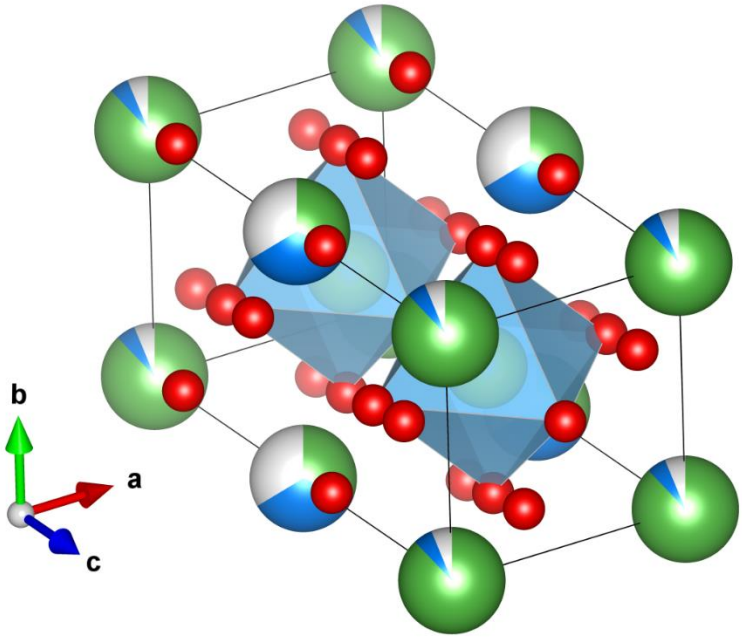

Figure 3: Crystal structure of LLTO ($Li_{0.21}La_{0.597}TiO_3$), Lithium and Lanthanum atoms are shown in dark blue and green spheres respectively, whereas yellow and red spheres indicate Titanium and Oxygen molecules.

2.3.2 NaSICON-type structure

NaSICON (sodium superionic conductors) have the general formula $NaA_2(BO_4)_3$ (where A is a metal such as Ti or Zr, and B is Si or P). Na can be replaced by Li to form NaSICON structured lithium ionic conductors. NaSICONs have covalent $[A_2(BO_4)_3]$ frameworks, containing AO_6 octahedra and BO_4 tetrahedral units, as shown in Figure 4. The framework is 3D connected and has interstitial sites available for ion motion. The size of the framework is correlated to the nature of the A site atom and carrier concentration [41]. Lithium-containing NASICON-structured materials are a promising class of solid-state Li-ion conductors for application in electrochemical energy storage devices. Amongst the wide variety of possible compositions the highest conductivities are reported for materials in which the substitution of tetravalent with trivalent metal cations leads to incorporation of additional lithium ions and a higher mobility of the charge carriers [79-82].

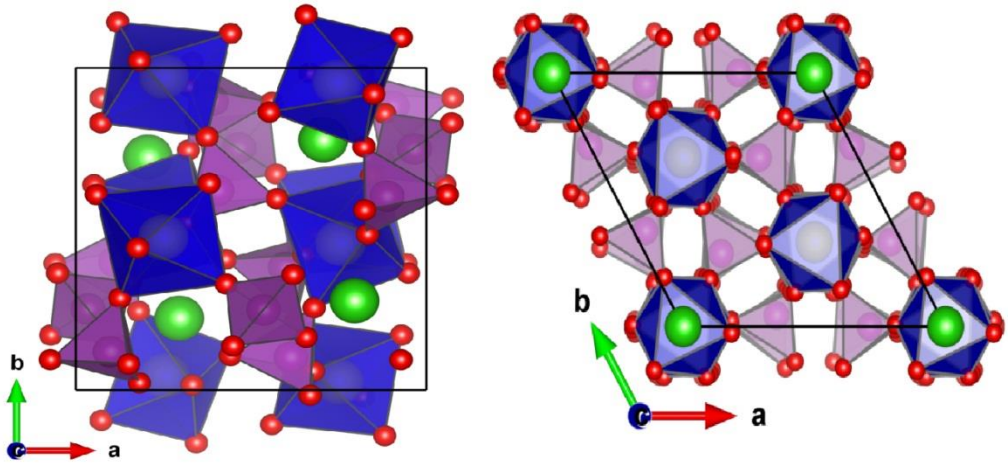

Figure 4 : Crystal structure of $LiZr_2(PO_4)_3$ monoclinic and rhombohedral phase along c-axis, ZrO_6 octahedra and PO_4 tetrahedra units are depicted in blue and purple respectively, green sphere depicts Li ions positioned in between two octahedra.

An Al substituted NaSICON, $Li_{1+y}AlyTi_{2-y}(PO_4)_3$ glass-ceramic has been commercialized. In addition Imanishi *et al.* found that LATP is stable in contact with lithium salt solutions [45, 46]. Using the LATP glass-ceramic membrane to protect the lithium anode directly enables the water-based batteries under development by PolyPlus Battery Corporation. However, as with LLTO, when this material is in direct contact with Lithium metal, Ti^{4+} is reduced to Ti^{3+}. Thus an interlayer between the lithium and glass ceramic LATP is required to prevent shorting [47].

2.3.3 Thio-LISICON Electrolyte

The Thio-LiSICON system was first determined by Kanno and coworkers [48, 49]. Replacement of oxygen by more polarizable sulfide ions in the framework enhances the ionic conductivity due to higher ion mobility. A crystal structure is provided in Figure 5. As an example, a RT ionic conductivity of 6.4 X 10^{-4} S cm^{-1} is reported for $Li_{3.4}Si_{0.4}P_{0.6}S_4$ [49], as compared to two orders lower conductivity (4.0 X 10^{-6} S cm^{-1}) of its oxygen counterpart $Li_{3.4}Si_{0.4}P_{0.6}O_4$ [50]. Due to its three-dimensional open framework structure, a record high ionic conductivity of 12 mS

cm^{-1} at RT which is higher even than the commercially liquid electrolytes, has been observed in $Li_{10}GeP_2S_{12}$ system [20]. Apart from exceptional ionic conductivity, sulfide-based system is easier to fabricate into dense structure and also has low interfacial resistance with common cathode materials. Toyota has successfully developed a solid battery system that is capable of 50 C rate charging and discharging using these materials as the solid electrolyte. Major disadvantages of this system are the incompatibility with many air and moisture which makes fabrication cumbersome.

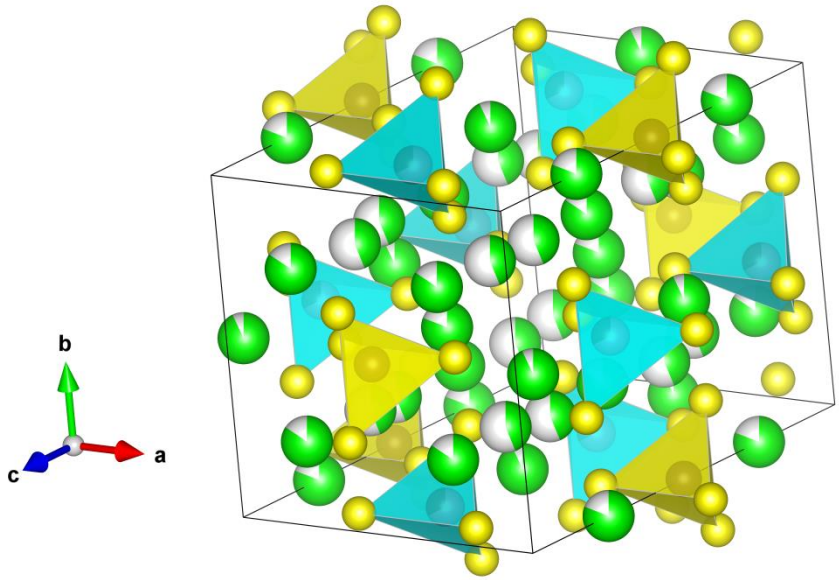

Figure 5: Crystal structure of thio-phosphate $Li_{0.35}P_{1.65}Si_{1.35}S_{12}$, PS_4 (yellow) represents tetrahedral units, and light blue represents Si polyhedra, yellow and green spheres represent S and Li atoms, respectively.

2.3.4 Amorphous inorganic solid electrolytes.

LIPON was first discovered by Bates *et al.* [51]. It is prepared by sputtering Li_3PO_4 in the N_2 atmosphere. It can be referred, as a lithium deficient glass with a nominal composition of $Li_{2.88}PO_{3.73}N_{0.14}$. The ionic conductivity is 3.3 X 10^{-6} S cm^{-1} at RT and has been used in thin film solid state battery configurations. Along life thin film solid state battery employing LIPON as the lithium-conducting

electrolyte with a minimum capacity loss after 1000 cycles has been demonstrated [52]. LIPON is generally accepted to be chemically stable with Li metal electrodes. However, Schwobel *et al*. reported the decomposition of LIPON into smaller units of Li_3P, Li_2O, Li_3N and Li_3PO_4 on contact with evaporated lithium [53]. Fabrication of thin films less than 10μm in thickness is another known issue with LIPON

2.3.5 Garnet Solid Electrolytes.

Garnet structures have a general formula of $A_3B_2(XO_4)_3$, where, A, B, and X are eight, six and four oxygen-coordinated sites. Li-stuffed garnets such as $Li_7La_3Zr_2O_{12}$ and $Li_5La_3Ta_2O_{12}$ contain more than three lithium per formula. These materials mostly crystallize in face-centered cubic structure; but tetragonal polymorphs are also known. Wepner and co-workers were first to explore the superior lithium ionic conductivity in garnet structure [54-57]. The RT ionic conductivity of $Li_5La_3M_2O_{12}$ (M=Ta, Nb) and $Li_6Al_2M_2O_{12}$ (A= Ca, Sr, Ba) phases is in the range of 10^{-5} S cm^{-1}. In 2007, the cubic garnet $Li_7La_3Zr_2O_{12}$ (LLZO) synthesized by Murugan et al., showed the lithium ionic conductivity of about 10^{-4} S cm^{-1} at RT [58]. Cubic LLZO is considered a promising solid electrolyte due to its high conductivity, and chemical stability against reduction by lithium metal. However, recent studies have shown that LLZO tends to react with CO_2 and forms Li_2CO_3 which results in lowered ionic conductivity. Synthesis of phase pure cubic LLZO phase is also comparatively more difficult than the tetragonal phase. Table 2 lists the typical room temperature ionic conductivity of a few selected electrolytes.

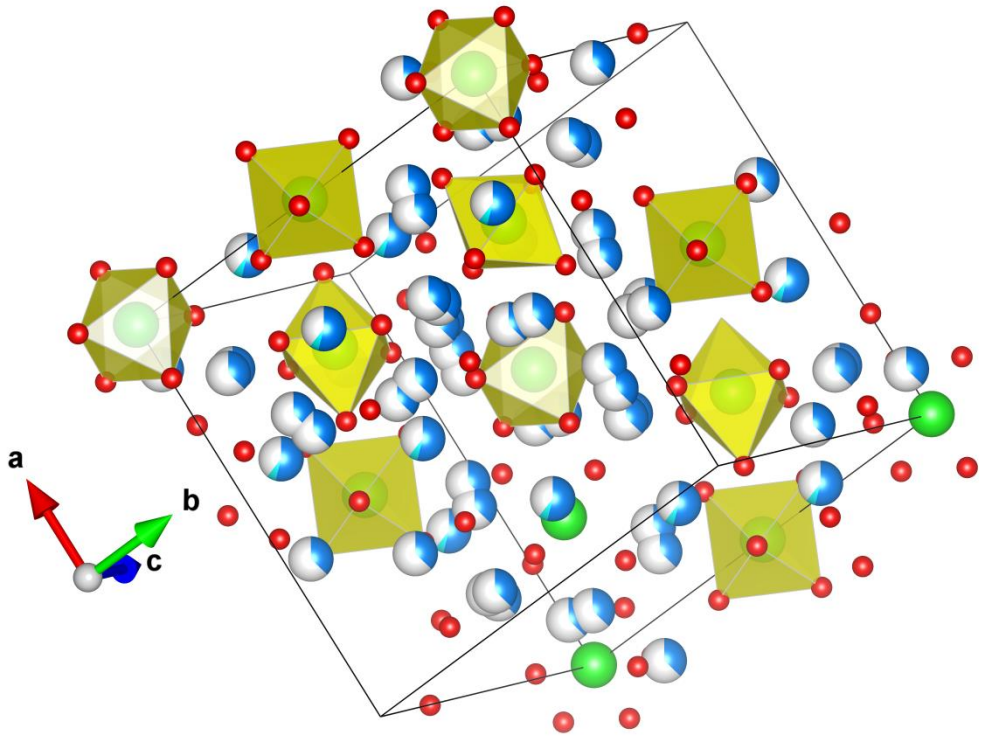

Figure 6: Crystal structure of LLZO garnet electrolyte, yellow polyhedral represents Zr octahedral, whereas dark blue and pink sphere represents Li and La atoms respectively and oxygen atoms are shown as red spheres.

Solid Electrolytes	Conductivity at 25 °C (S/cm)
$Li_7La_3Zr_2O_{12}$	$3X10^{-4}$ [59]
$Li_{1.3}Al_{0.3}Ti_{1.7}(PO_4)_3$	$1.3X10^{-3}$ [46]
$Li_{0.34}La_{0.51}TiO_{2.94}$	$1.4X10^{-3}$ [40]
$Li_{2.88}PO_{3.73}N_{0.14}$	$3.3X10^{-6}$ [52]
$Li_{3.4}Si_{0.4}P_{0.6}O_4$	$4.3X10^{-6}$ [51]
$Li_{10}GeP_2S_{12}$	$1.2X10^{-2}$ [20]

Table 2: Conductivities at 25 °C of various solid-state electrolytes.

2.4 Objectives of the present thesis.

The objective of this thesis work is to:

- Synthesize various polymorphs of Lithium Zirconium Phosphate.
- Study the Li^{+} conductivity in synthesized polymorphs of pure LZP
- Effect of $(SiO_4)^{4-}$ on the crystal structure and ionic conductivity of various polymorph

Chapter 3

Fabrication of $LiZr_2(PO_4)_3$ ceramics

3.1 Introduction to NaSICON-type LZP.

The use of lithium metal as the negative electrode coupled with a high capacity positive electrode such as sulfur or air would theoretically enable exceptionally high energy density devices which would pave the way for their use in large formats application (electric vehicle, for example).

However, the extreme reactivity of metallic lithium with most liquid electrolyte solutions is a serious safety and viability concern as the dendrite growth of lithium could result in the battery explosion. The use of a solid electrolyte as a lithium ion conducting separator is considered one way to enable a metallic lithium electrode in lithium batteries. This could be realized only if the solid electrolyte has the desired high conductivity and electrochemical stability. Among the ceramic electrolytes that have been studied, the NaSICON-type $LiZr_2(PO_4)_3$ is promising due to its fast ion transport of the order of 10^{-4} to 10^{-5} Scm^{-1}.

NaSICON-type compounds possess a number of properties of practical interest, in particular, high ionic conductivity and thermal stability, low thermal conductivity, and weak thermal expansion [59]. These compound possess general formula as $NaZr_2(PO)_4$. NaSICON and related phases are of interest in various fields of research such as solid electrolytes and cathode materials for lithium-ion batteries, ultra-low expansion ceramics, and immobilization of ^{137}Cs, ^{90}Sr related nuclear waste [60] [61].

The term NaSICON, which stands for Na^+ *Super Ionic Conductor*, was given to the solid solution phase $Na_{1+x}Zr_2Si_xP_{3-x}O_{12}$, x=2.0, discovered by Hong and Goodenough in 1976 [62, 63]. The end member $NaZr_2(PO_4)_3$ has very low ionic conductivity, but it can be increased substantially on aliovalent doping, rising to

of 2 X 10^{-1} S cm^{-1} at 300 °C for x=2.0, comparable to that of sodium-beta alumina. The lithium-containing analogues, $LiM_2(PO_4)_3$ with M^{4+} = Zr [64-71], Ge [64, 69, 72, 73] and Hf [61, 64, 69, 74] also have NaSICON-type structures. Figure 7 depicts the crystal structure of $LiZr_2(PO_4)_3$ rhombohedral phase where corner spaces are captured by ZrO_6 octahedral and PO_4 tetrahedral units creating two types of crystal sites for lithium ions, commonly referred to as M1 and M2; the M1 sites are situated between pairs of ZrO_6 octahedra along c-axis, while the M2 sites are located between infinite ribbons of $[O_3ZrO_3M1O_3ZrO_3M1O_3ZrO_3M1]$. Lithium in $LiZr_2(PO_4)_3$ is reported to be selectively occupying the M1 sites, but in some cases, it also occupies (at least partially) another site M3 that lies halfway between M1 and M2. Lithium intercalation in the material, however, is achieved by filling of the M2 cavities, which is associated with the cooperative migration of $L1^+$ ions from the M1 to the M2 site A good tunneled path can be observed supporting Li-ion conduction through it.

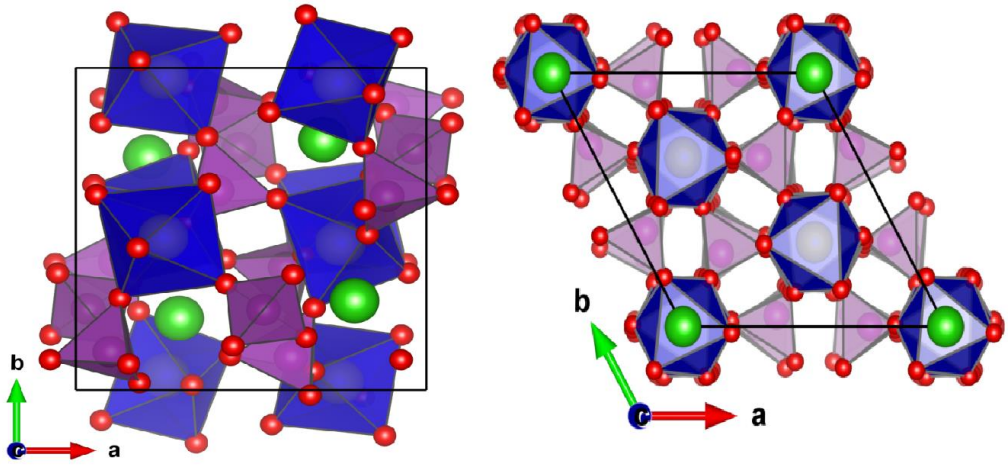

Figure 7: Crystal structure of $LiZr_2(PO_4)_3$ monoclinic and rhombohedral phase along c-axis showing Zirconium (dark blue) and Phosphorous (purple) polyhedra.

But syntheses of these compounds present a number of problems, especially in case of Li compounds. In particular, the high conductivity rhombohedral phase of these compounds can only be synthesized at high temperatures [75], where Li-containing starting reagents may vaporize, resulting in uncontrolled lithium losses

and hence, deviation from the desired stoichiometry. This results in the formation of impurity phases which can segregate at the grain boundaries decreasing the grain boundary (and overall) conductivity.

$LiZr_2(PO_4)_3$ exists in some polymorphs. Two main polymorphs of LZP can be accessed depending on the synthesis temperature namely, β and α-type phases. β-type phases, prepared at 900 °C, are monoclinic with a β-$Fe_2(SO_4)_3$ type structure; whereas α-type phases, prepared at higher calcination temperatures around 1300 °C is rhombohedral. Despite the complex polymorphism of $LiZr_2(PO_4)_3$, it is generally found that the material has a bulk conductivity ~ 1 X 10^{-4} S cm^{-1} when the rhombohedral α-phase is stabilized. The ionic conductivity data for $LiZr_2(PO_4)_3$ suggested that order-disorder transition between these phases occurs near 60 °C [75]. The cation arrangement in the high temperature (rhombohedral) phase is markedly less ordered [76, 77]. Partial heterovalent substitution of penta- or trivalent cations for zirconium, accompanied by the formation of cation vacancies or interstitials, increases the mobility of lithium ions and reduces the temperature of the triclinic to a rhombohedral phase transition.

3.2 Synthesis Methods.

3.2.1 Synthesis of $Li_{(1+x)}Zr_2(P_{(1-x)}Si_xO_4)_3$ (x=0, 0.05, 0.1 ceramics.

A citrate-based sol-gel route was used for the synthesis of LZP. Starting precursors Lithium Carbonate (Li_2CO_3), Zirconium propoxide ($Zr(OCH_2CH_2CH_3)_4$), and Ammonium Phosphate ($NH_4H_2PO_4$) according to the stoichiometric ratio. Initially, $NH_4H_2PO_4$ was dissolved in doubly deionized water while stirring continuously with the help of a magnetic stirrer. Then, the stoichiometric amount of Li_2CO_3 was dissolved in dilute nitric acid, and the solution was added to the aqueous solution of $NH_4H_2PO_4$. 10% of excess lithium carbonate was used to compensate for lithium losses during the high-temperature calcination. Finally, $Zr(OCH_2CH_2CH_3)_4$ was added to the mixed aqueous solution of Li_2CO_3 and $NH_4H_2PO_4$. In addition to all these, Tetraethyl orthosilicate

($Si(OC_2H_5)_4$) was used as the precursor for fabrication of doped ceramics. To this mixture, certain amount (approximately 1 g) of citric acid and ethylene glycol (in 1:1 molar ratio) were added. After stirring this sol for 5 hours, a gel was obtained which was dried at 120 °C. A summary of the powder processing is provided in a schematic shown in Figure 8. The stoichiometric amount of all the precursors used in the fabrication of different ceramics are shown in Table 3.

Precursors	Pure LZP	5% doped LZP	10% doped LZP
Lithium Carbonate (Li_2CO_3)	0.4284g.	0.3935g.	0.4444g
Zirconium propoxide ($Zr(OCH_2CH_2CH_3)_4$)	9.8862g	7.8828g	7.8727g
Ammonium Phosphate ($NH_4H_2PO_4$)	3.6378g	2.7614g	2.6124g
Tetraethyl orthosilicate ($Si(OC_2H_5)_4$)	-	0.2632g	0.5257g

Table 3: Amounts of precursors used for fabrication of ceramics.

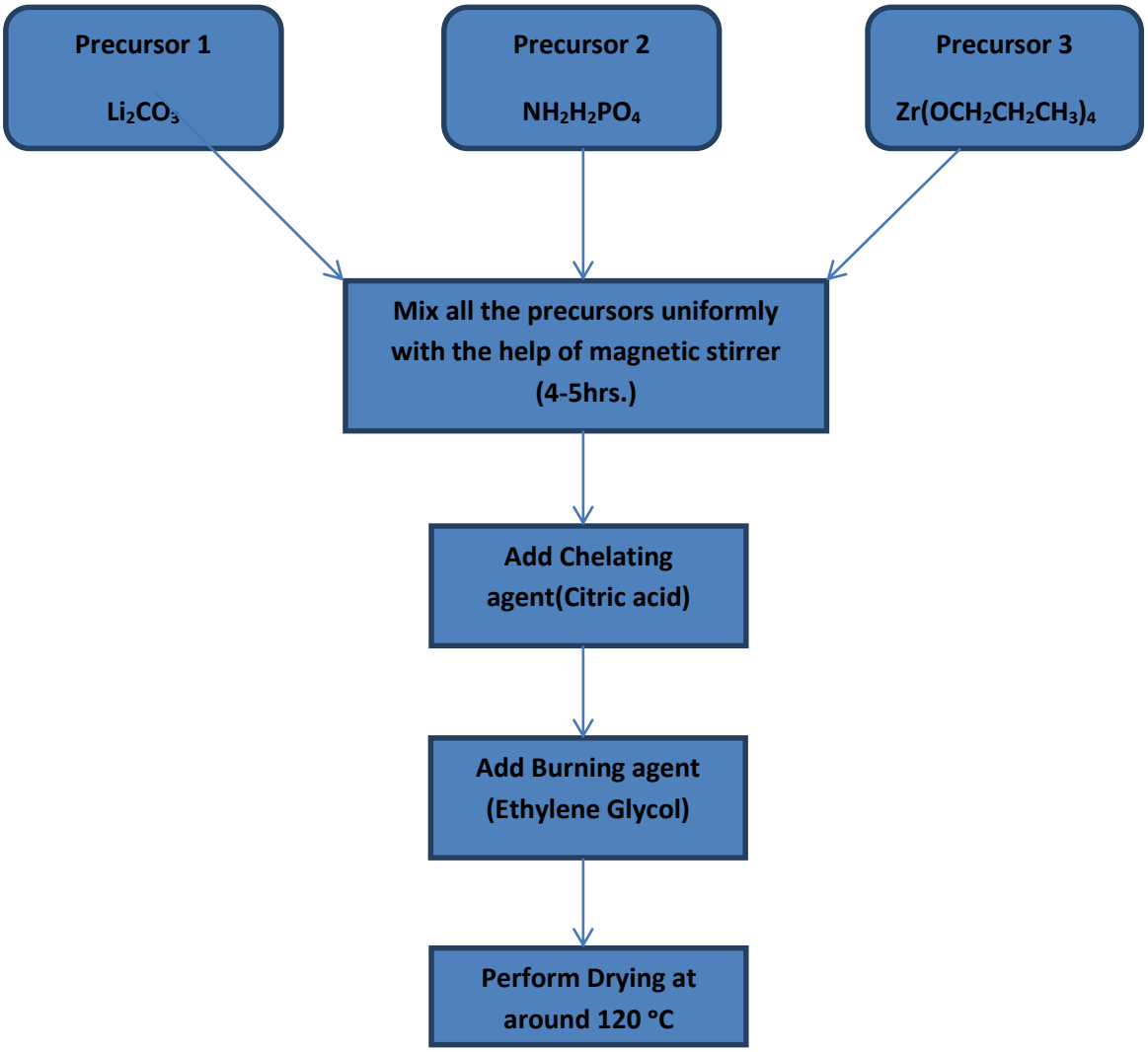

Figure 8: Schematic of $LiZr_2(PO_4)_3$ powder processing.

This gel was heated at 500 °C for 6 hours and subsequently at 700 °C for 6 hours. The resulting powder was thoroughly ground using a mortar and pestle. Figure 9 shows the process required in the fabrication of pellets. Pellets around 1-2 mm thick were made by cold uniaxial pressing of powders using a stainless steel die of 10mm diameter. The pressed pellets were then placed in a covered alumina crucible, and sintered at 900 °C for 12 hours and 1300 °C for 24 hours to obtain the desired phase, *viz.* monoclinic (LZP-00-M, LZPS-05-M and LZPS-10-M) and rhombohedral (LZP-00-R, LZPS-05-R and LZPS-10-R) respectively. The surfaces of the sintered pellets were dry-polished using a polishing paper/emery sheet with grit number of 800 and 1000, removing certain thickness from either surface to remove the contamination from the alumina crucible.

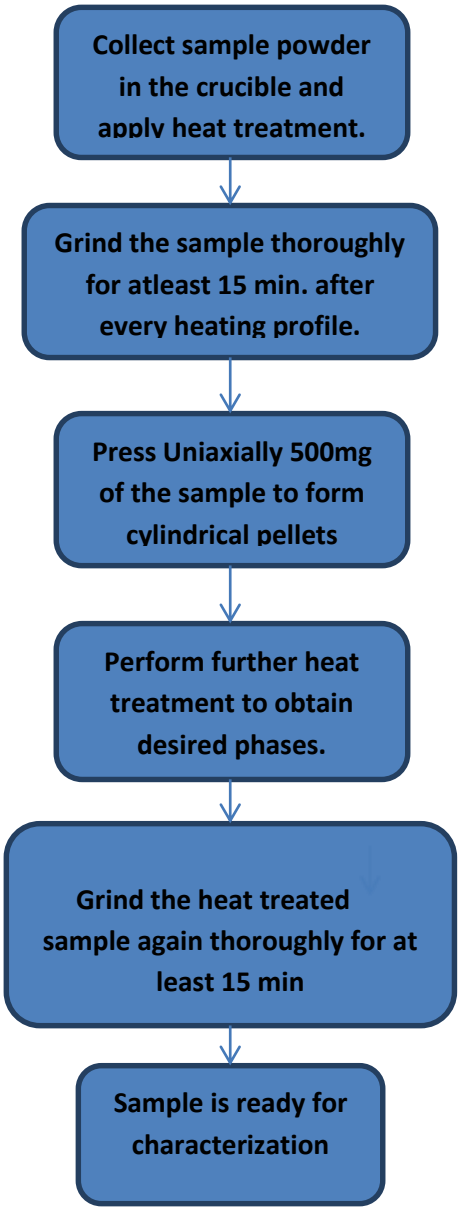

Figure 9: Process Flowchart for fabrication of pellets.

3.3 X-ray Powder Diffraction.

X-ray powder diffraction is a popular tool to obtain the information of atomic structure from solids such as space group, lattice constants, atomic positions, etc., of crystals. In a crystal, since the inter-planar spacing is generally of the order of several angstroms (Å), the atomic planes can diffract electromagnetic waves, like X-rays, whose wavelength is comparable to the inter-planar spacing. A monochromatic X-ray beam will be diffracted if the Bragg condition (equation 1) is satisfied:

$$n\lambda = 2dsin\theta \qquad (1)$$

where n is an integer that provides the order of diffraction, λ is the X-ray wavelength, d is the inter-planar spacing, and θ is the glancing angle between the incident beam and the scattering atomic planes. In practice, the diffraction angle is commonly specified as 2θ rather than θ.

It is well known that in the crystal materials there are long-range periodic structures, and thus Bragg's law is appropriate. Therefore, crystal materials produce an X-ray or electron diffraction patterns with sharp Bragg peaks. In the present study, nature of solid electrolyte was characterized by X-ray powder diffractometry (XRD) using Cu-Kα radiation (λ = 1.54178Å) using Bruker-D2 Phaser diffractometer. XRD data were collected in the 2θ range 10-60° with a step size of 0.02° at RT. It is expected that sharp Bragg peaks are observed for the electrolyte materials.

3.4 Density Measurement.

The density of solid electrolyte was measured using the samples' dimensions and weights.

The most general definition of density is mass per unit volume. Density can vary throughout the body if the mass is not distributed uniformly. If the mass of

an object is distributed uniformly throughout the object, the density ρ is defined as the total mass M divided by the volume V of the object. In equation form (equation 2) this is expressed as:

$$\rho = \frac{M}{V} \qquad (2)$$

While using Vernier caliper, initially the dry weights of solid electrolyte samples were determined, (say M). Since the samples were formed in the form of cylindrical pellets, their Thickness and Diameter were determined using Vernier caliper. For each sample, the thickness and diameter value has been determined by taking the average of 5 measurements. Finally, the density was calculated using these directly measured values. For a cylinder, the volume (equation 3) is given by:

$$V = \pi d^2 L/4 \qquad (3)$$

Where L is the length or thickness of the pellet, and d is the diameter of the pellet. The density (equation 4) of the pellet is then determined using:

$$\rho = 4M/\pi d^2 L \qquad (4)$$

An error of ±2% is associated with final value due to the flatness of pellet surface as well as the least count of weighing balance and Vernier caliper.

3.5 Scanning Electron Microscopy.

Scanning Electron Microscopy (SEM) is a widely used technique in materials research. SEM uses a high-energy beam of incident (or primary) electrons for scanning the specimen surface to create 3-dimensional images (micrographs). The primary electrons are normally accelerated through a potential of 10-200 keV. When the primary electrons hit the specimen surface, their interaction with the

specimen can be both elastic and inelastic. Back-scattered electrons (BSE) are the high-energy electrons (E_{BSE} > 50 eV) generated from an elastic interaction between the primary electrons and nuclei of specimen atoms. Secondary electrons (SE) are lower-energy electrons (E_{BSE} <= 50 eV) produced by an inelastic interaction between the primary electrons and electrons of specimen atoms. These SE electrons are actually the valence electrons bombarded out of specimen atoms by the high-energy primary electron beam. In SEM, micrographs are often created from SE node.

In the present work, a Supra 55 Zeiss field emission scanning electron microscope (FE-SEM) was used to study the microstructure of the sintered pellets.

3.6 Complex Impedance Analysis.

To understand ion conduction mechanism, the most straightforward technique is the direct measurement of electrical conductivity. A particular problem when applying a DC bias to a sample *via* two standard metal electrodes is polarization at the electrodes due to the failure of the mobile ions to traverse the electrolyte/electrode interface (ionic currents drops to zero). This problem may, in some cases, be solved by special four probe DC techniques such as the van der Pauw method, or two reversible electrodes (e.g. mixed conductors) which will allow ion transport across the electrolyte/electrode interface. Nevertheless, AC techniques are generally simpler and more applicable to conductivity techniques than their DC counterparts.

In AC impedance measurement, a small potential perturbation is applied to the sample. The AC response to the applied perturbation, which is normally sinusoidal, can be different in phase and amplitude from the applied signal. Data from the measurement must be collected at short times; otherwise, diffusion rather than kinetics becomes the rate determining process. Measurements of the phase difference and the amplitude (i.e., impedance) allow the analysis of the electrode process relating to contributions diffusion, kinetics, double layer capacitance, coupled with homogenous reactions, etc. It is widely applied in studies of ionic

solids, solid electrolytes, conducting polymers, corrosion, membranes and liquid/liquid interfaces.

Electrochemical impedance is generally measured by applying an AC potential to an electrochemical cell and then measuring the AC through the cell. Assume that a sinusoidal potential:

$$E(t) = E_o \exp(jwt) \qquad (5)$$

Is applied. Then the AC corresponding to thus potential can be expressed as follows:

$$I(t) = I_o \exp(jwt - j\psi) \qquad (6)$$

The complex impedance (Z) can be determined by:

$$Z = \frac{E}{I} = Z_o \exp(j\psi) = Z_o(\cos\psi + j\sin\psi) \qquad (7)$$

Where w is the frequency, and ψ is the phase difference between the applied potential and response current.

As seen from equation 7, the expression for Z (w) consists of a real and an imaginary part. If the real part (Z′) and the imaginary part (Z″) multiplied by -1 is presented on the X-axis and the Y-axis respectively, a "Nyquist plot" is obtained, as shown in the Figure 10. It should be noticed that in the Nyquist plot of electrochemical impedance spectroscopy data each point corresponds to the impedance at one specific frequency; low-frequency data are on the right-hand side, while those of higher frequencies are on the left-hand side of the plot.

For solid electrolyte material, the Nyquist plot generally looks like Figure 11. The Equivalent Circuit of Figure 11 is shown in Figure 12. C_b is the geometric capacitor between the electrodes; CPE is a constant phase element due to the polarization distribution at the interface between the blocking electrodes and the

electrolyte. Normally, we are mostly interested in R_b which characterizes the DC bulk resistance of the solid electrolyte material.

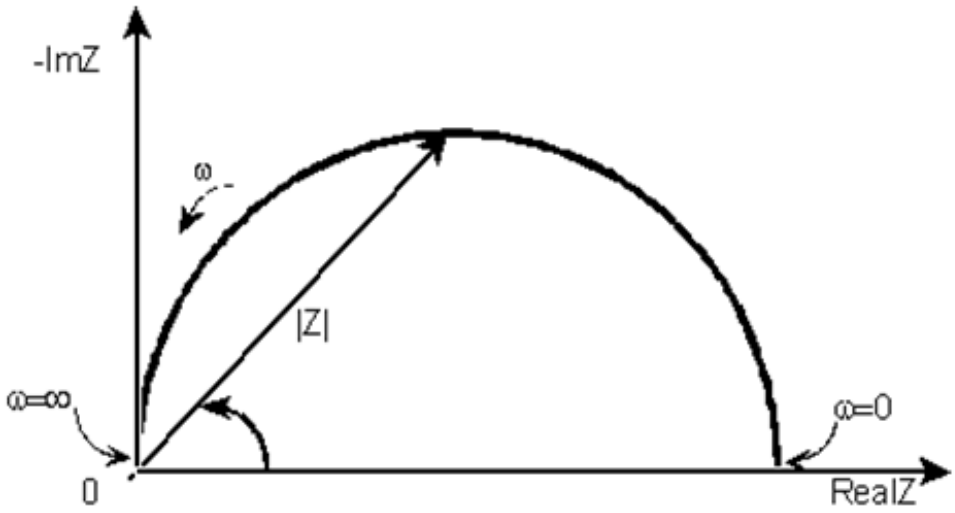

Figure 10: Nyquist plot with impedance vector.

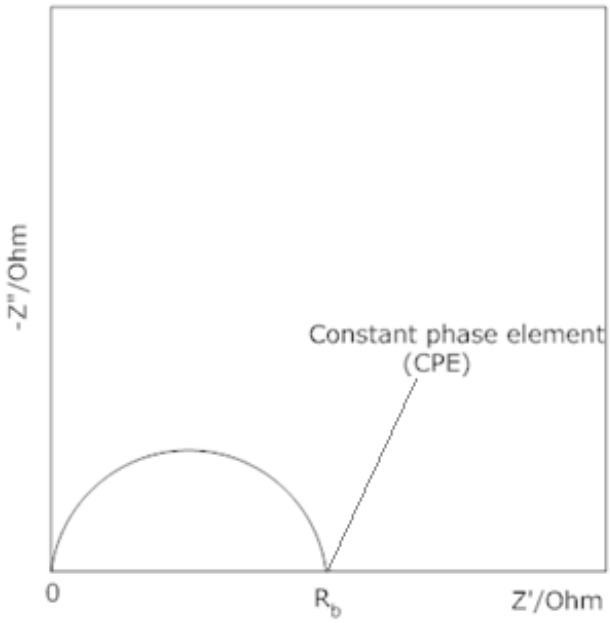

Figure 11: Nyquist plot of impedance for the solid electrolyte with bulk conductivity and ion blocking electrodes.

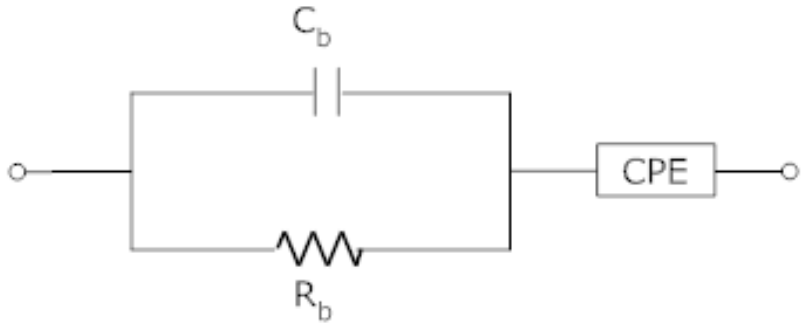

Figure 12: Equivalent circuit of figure 11 with ion blocking electrodes.

In Polycrystalline materials, the Nyquist plot is generally described as Figure 13 and the corresponding equivalent circuit looks the one given in like Figure 14. C_b and R_b are the capacitance and resistance attributed to the bulk, respectively. C_{gb} and R_{gb} are the capacitance and resistance due to grain boundary, and CPE is due to the polarization distribution at the interface between the electrolyte and ion blocking electrodes.

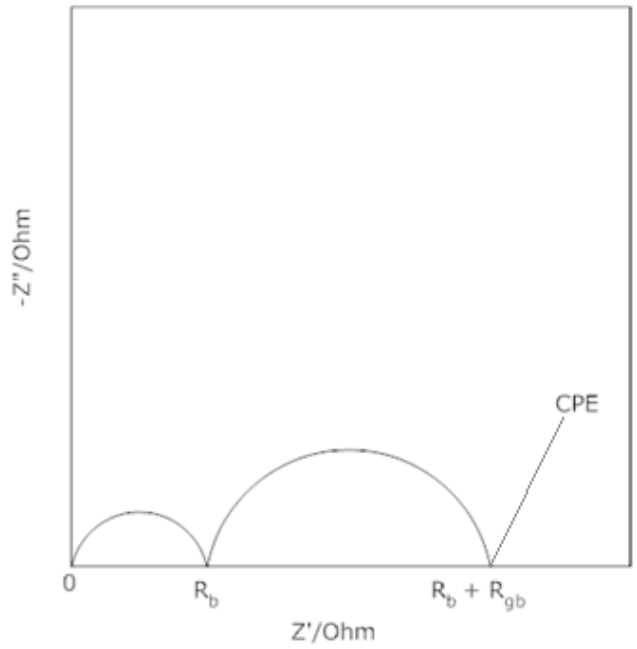

Figure 13: Nyquist plot of impedance for polycrystalline solid electrolyte with ion-blocking electrodes.

The situation is comparable to brick-layer model that has been derived for polycrystalline samples with highly conducting grain boundaries. This model

distinguishes bulk, space charge layers, and grain boundary regions. The high-frequency semicircle then includes both contributions from bulk and the space charge zones of the parallel grain boundaries. The in-series contributions from the perpendicular grain boundary core appear as a separate low-frequency semicircle, and CPE is due to the polarization distribution at the interface between the electrolyte and ion blocking electrodes. Figure 14 shows the equivalent circuit for the situation.

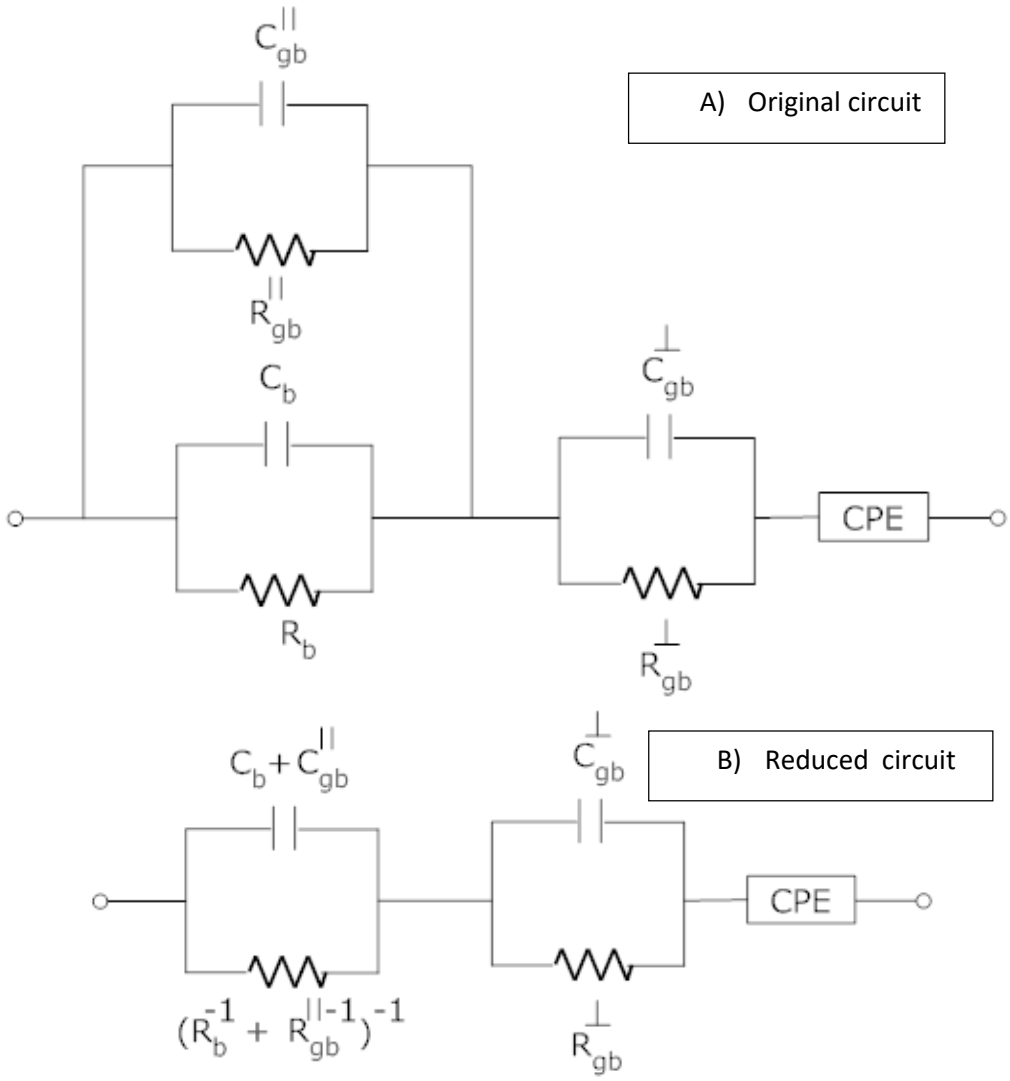

Figure 14: Equivalent circuit of figure 13 according to Brick-layer model.

In this study, for electrical property measurements, surfaces of pellets were polished flat, and then silver electrodes were painted on either side. Impedance Spectroscopy/AC impedance measurements (EIS) were obtained on dense pellets

using a computer controlled ZM2376 LCR Meter (NF Corporation) by applying a sinusoidal signal with 1.0V amplitude. Measurements were made at various frequencies in the range from 1Hz to 1MHz. Resistances were determined from the intercepts of the relevant capacitive arcs at the real axes in the Nyquist Plots and conductivities calculated using the equation:

$$\sigma = (1/R)\,(L/A) \qquad (8)$$

where R is the DC resistance calculated from the intercept of low-frequency semi-circle on the x-axis, L is the pellet thickness, and A is the pellet area. Typical pellets were around 1-2 mm thick, and 8-9 mm in diameter. Activation energies were determined from the behavior of the conductivity as a function of temperature using the Arrhenius equation:

(9)

where σ is the bulk ionic conductivity of the material which is measured in ohm^{-1} m^{-1}, σ_o is the intercept of the plot on the y-axis, E_A gives the activation energy value, k_B is the Boltzmann constant with a constant value of 8.617 X 10^{-5} eV $K^{-1,}$ and T is the temperature in Kelvin.

Chapter 4

RESULTS AND DISCUSSION.

4.1 DENSITY MEASUREMENT.

In measuring density value of the samples, weight, thickness, and diameter of pellets were determined first. Table 4 shows the obtained weights, Thickness and Diameter of different sample pellets for both monoclinic (denoted by M) and rhombohedral (denoted by R). Also, same values were used for the calculating the Density value using equation 4.

Sample	LZP-00		LZPS-05		LZPS-10	
	M	R	M	R	M	R
Weight (g.)	0.1961	0.2200	0.2470	0.3370	0.2293	0.2723
Thickness (mm.)	1.419	1.658	1.499	2.063	1.332	1.718
Diameter (mm.)	10.085	8.778	9.200	8.795	9.201	8.370
Density (g/cm^3)	1.73	2.19	2.49	2.69	2.60	2.89

Table 4: Obtained weights, thickness, and diameter value of the different sample. Densities of all samples were calculated using equation 4.

From the measured density value, it can be inferred that rhombohedral phase of a particular sample is denser than its monoclinic analogous. Also it can been seen that, with the increase in content of $(SiO4)^{4-}$ in the general formula, $Li_{1+3x}Zr_2(P_{1-x}Si_xO_4)_3$, the density value also increases, i.e., for x = 0 to x = 0.1 , the density value increases from 1.73 g/cm^3 to 2.60 g/cm^3 in the monoclinic phase whereas it increases from 2.19 g/cm^3 to 2.89 g/cm^3 for the rhombohedral phase.

4.2 X-ray Diffraction Analysis

Structural investigation of the $LiZr_2(PO_4)_3$ samples were carried out with X-ray diffraction technique. The structural parameters at RT were obtained from the Bruker-D2 phaser diffractometer with Cu-Kα radiation in the 2θ ranges

of 10-70°, step size of 0.02°. The lattice parameters were deduced by fitting the XRD patterns with TOPAS 3.0 software and atomic

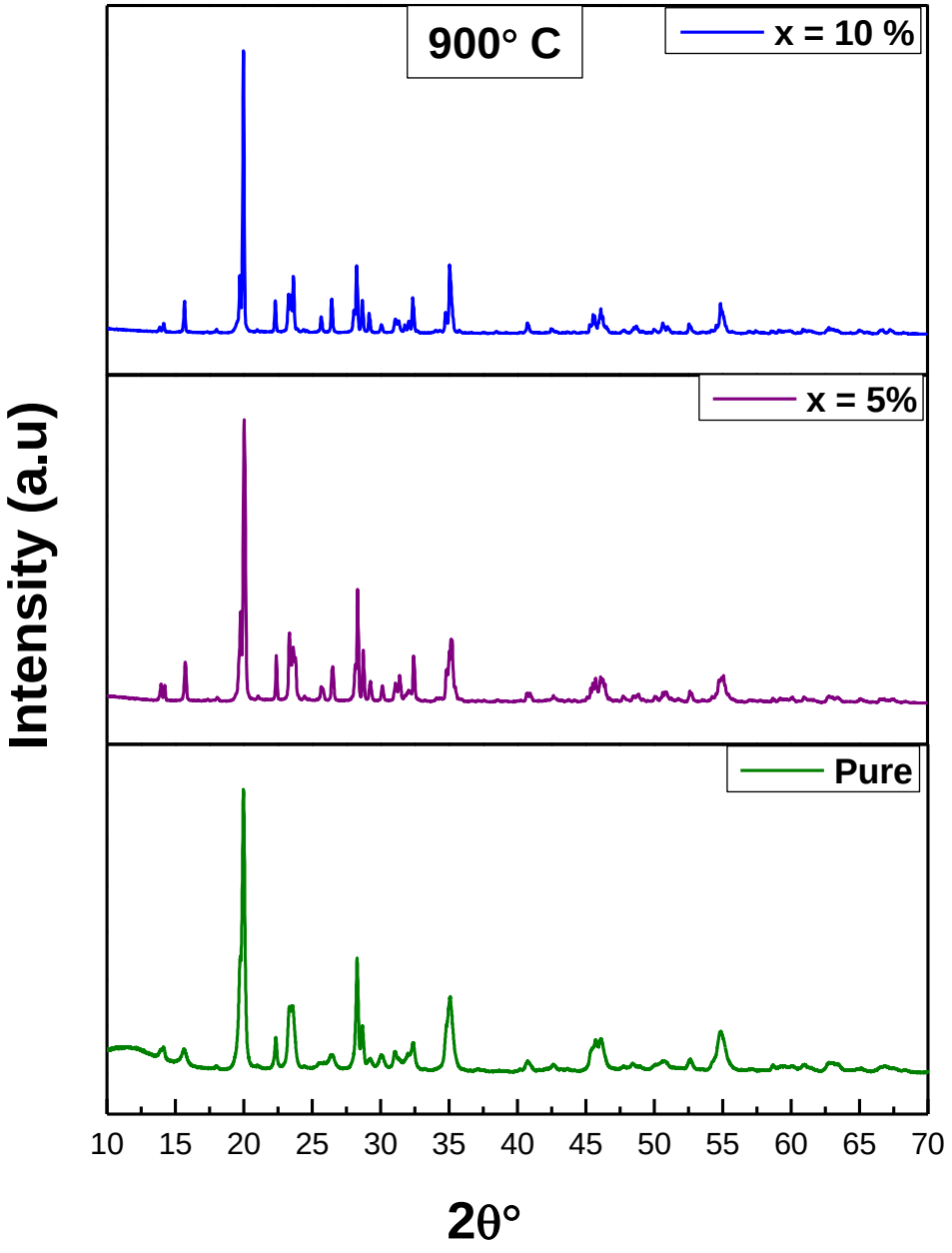

Figure 15: X-ray diffraction patterns of $Li_{1+3x}Zr_2(P_{1-x}Si_xO_4)_3$ (x = 0, 0.05 and 0.1) samples sintered at 900 °C.

coordinates reported by Catti et al. for α- $LiZr_2(PO_4)_3$ and β- $LiZr_2(PO_4)_3$ were used as starting model for the refinement for LZP-R and LZP-M respectively.

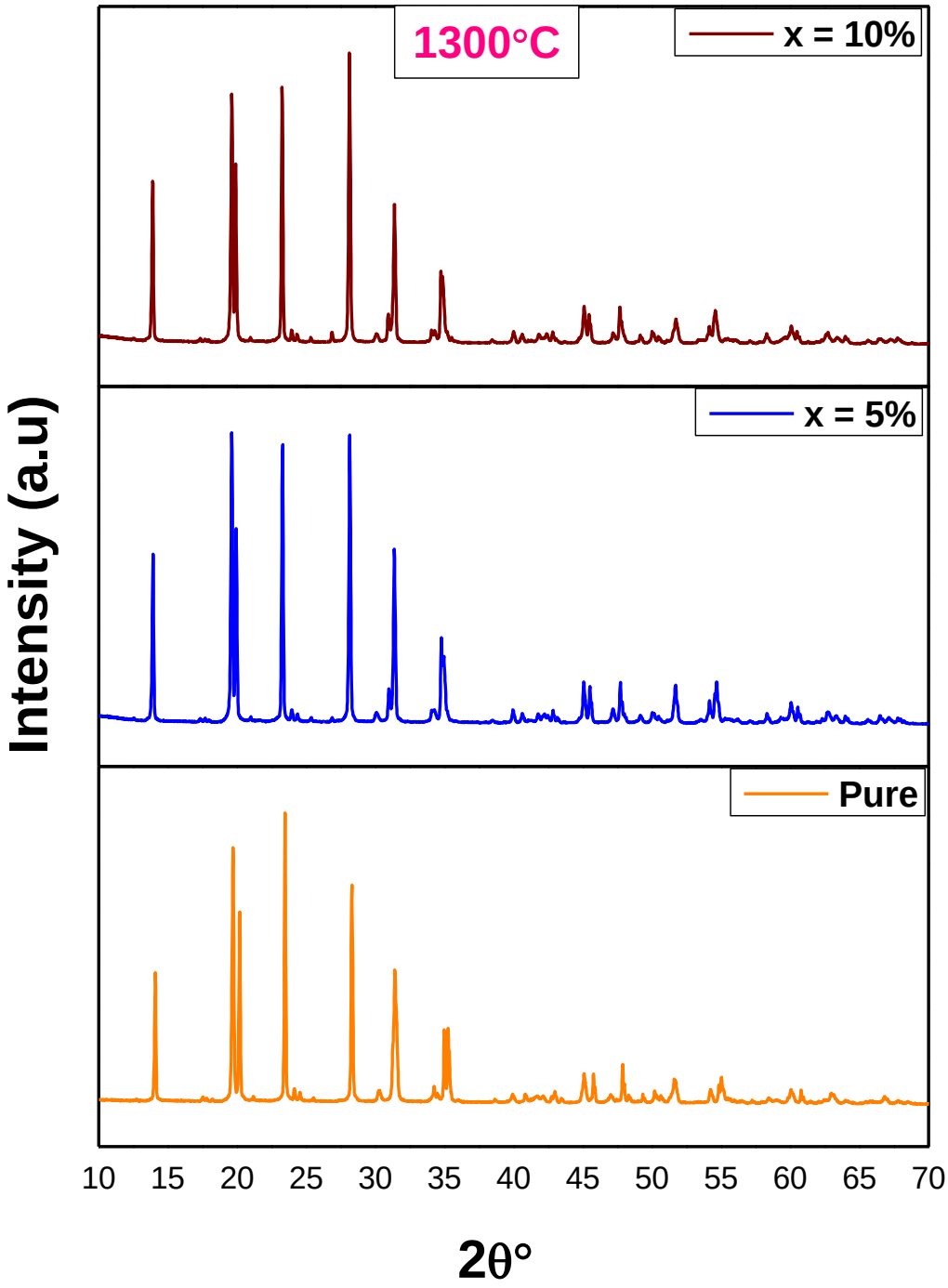

Figure 16: X-ray diffraction patterns of $Li_{1+3x}Zr_2(P_{1-x}Si_xO_4)_3$ (x = 0, 0.05 and 0.1) samples sintered at 1300 °C.

Figure 15 and Figure 16 shows the XRD pattern of $Li_{1+3x}Zr_2(P_{1-x}Si_xO_4)_3$ (x = 0, 0.05 and 0.1) samples sintered at 900 °C for 12 hours and 1300 °C for 24 hours respectively. Pure β phase LZP was obtained at 900 °C, all the samples crystallize in the monoclinic system ($P2_1/n$). The rhombohedral structure of LZP is required to achieve a high conductivity. When the sintering temperature further increased from 900 °C to 1300 °C, the peaks belonging to α-phase appeared. Finally, β phase totally transformed into α phase with the heating condition of 1300 °C for 24 hours. Therefore, high temperature and long dwell time are necessary to achieve the high conductivity rhombohedral phase.

From both the XRD patterns, it is found that all the peaks could be indexed to a single phase of the monoclinic crystal structure with $P2_1/n$ space group and rhombohedral structure with $R\bar{3}c$ space group. No major peaks related to the impurity phases had been detected in these spectra. Thus, we conclude that phase purity series of $Li_{1+3x}Zr_2(P_{1-x}Si_xO_4)_3$ (x = 0, 0.05 and 0.1) synthesized successfully.

Figure 17 (a) $LiZr_2(PO_4)_3$ pure 900 °C, (b) $LiZr_2(PO_4)_3$ pure 1300 °C, Figure 18 (a) $Li_{1.15}Zr_2(P_{0.95}Si_{0.05}O_4)_3$ doped 5% 900 °C, (b) $Li_{1.15}Zr_2(P_{0.95}Si_{0.05}O_4)_3$ doped 10% 1300 °C, Figure 19 (a) $Li_{1.3}Zr_2(P_{0.9}Si_{0.1}O_4)_3$ doped 10% 900 °C, (b) $Li_{1.3}Zr_2(P_{0.9}Si_{0.1}O_4)_3$ doped 10% 1300 °C, shows the Rietveld refinements of room temperature X-ray diffraction (XRD) data prepared at both 900 °C and 1300 °C. Symbol (open circle), solid line (in red color) and bottom line (in gray color) represent the observed, calculated, and the difference profiles. The bottom vertical bars represent the 2θ position of all possible Bragg reflections in space groups $P2_1/n$ and $R\bar{3}c$.

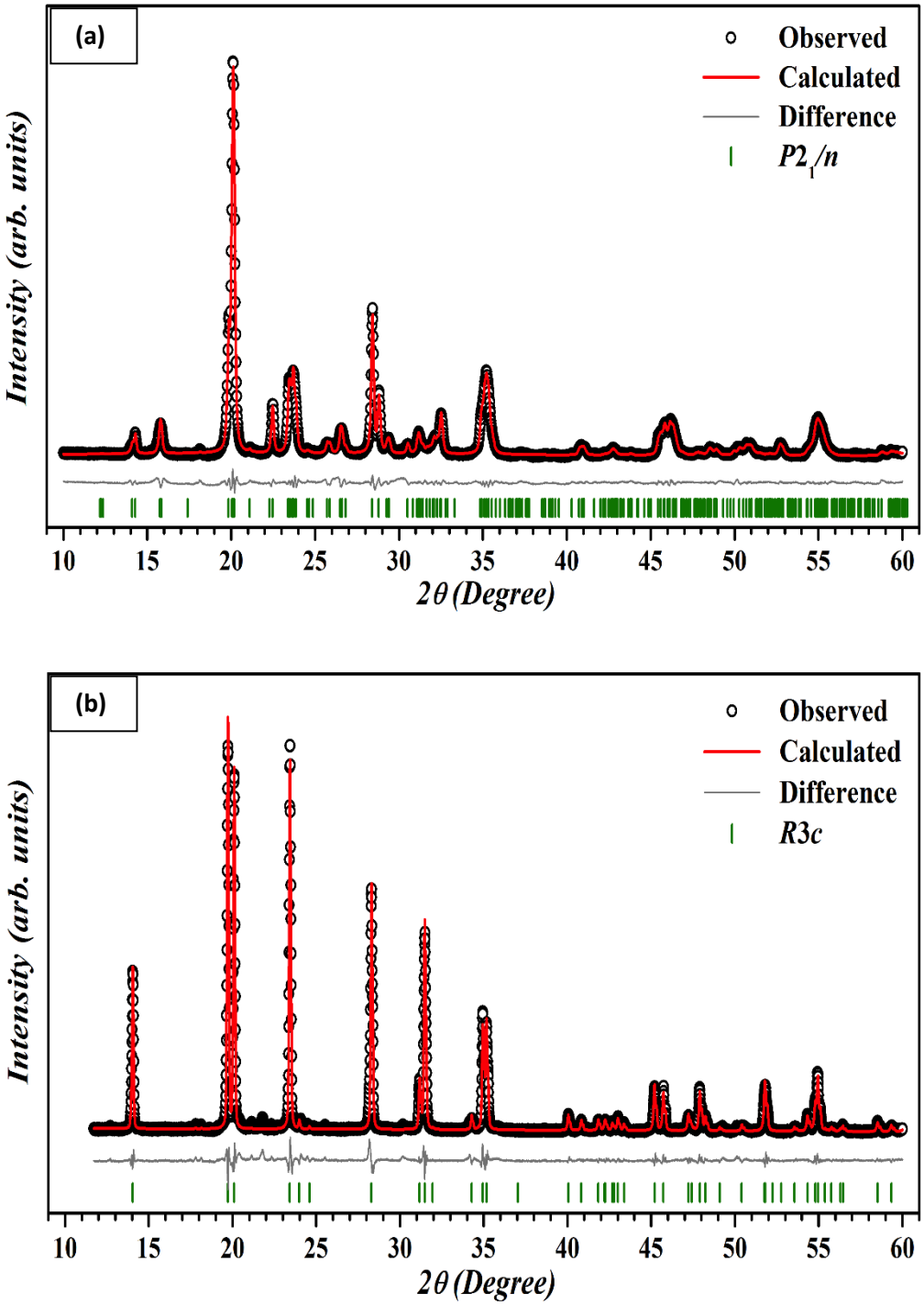

Figure 17: Rietveld refinement of powder XRD patterns for LZP-00-M (a) and LZP-00-R (b). The open circle symbols are observed data points, the solid lines are the refinement result, and bottom lines represent the difference in the observed and calculated plot. The vertical bars are the Bragg positions of the reflections in the space group $P2_1/n$ (a) and $R\bar{3}c$ (b).

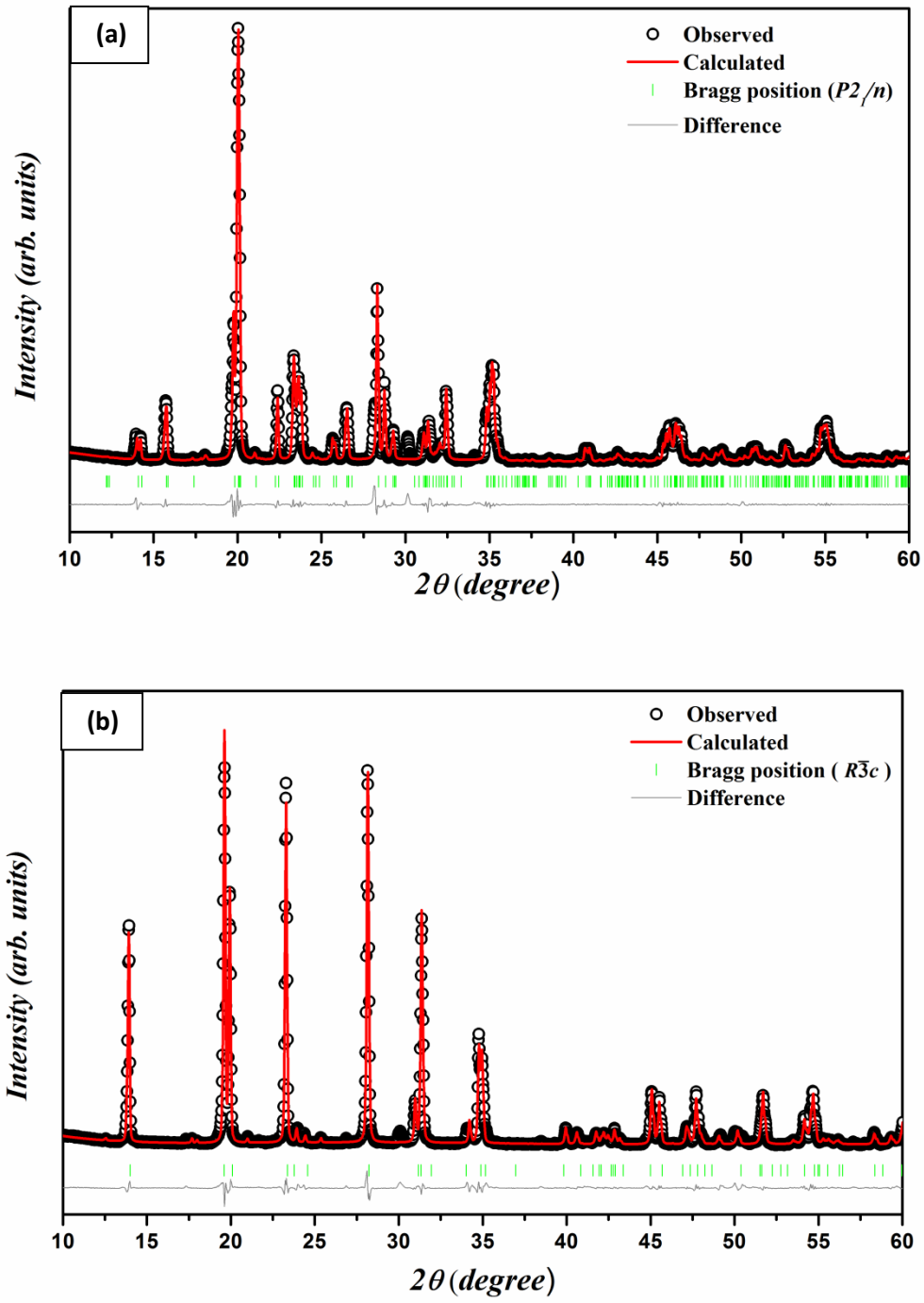

Figure 18: Rietveld refinement of powder XRD patterns for LZP-05-M (a) and LZP-05-R (b). The open circle symbols are observed data points, the solid lines are the refinement result, and bottom lines represent the difference in the observed and calculated plot. The vertical bars are the Bragg positions of the reflections in the space group $P2_1/n$ (a) and $R\bar{3}c$ (b).

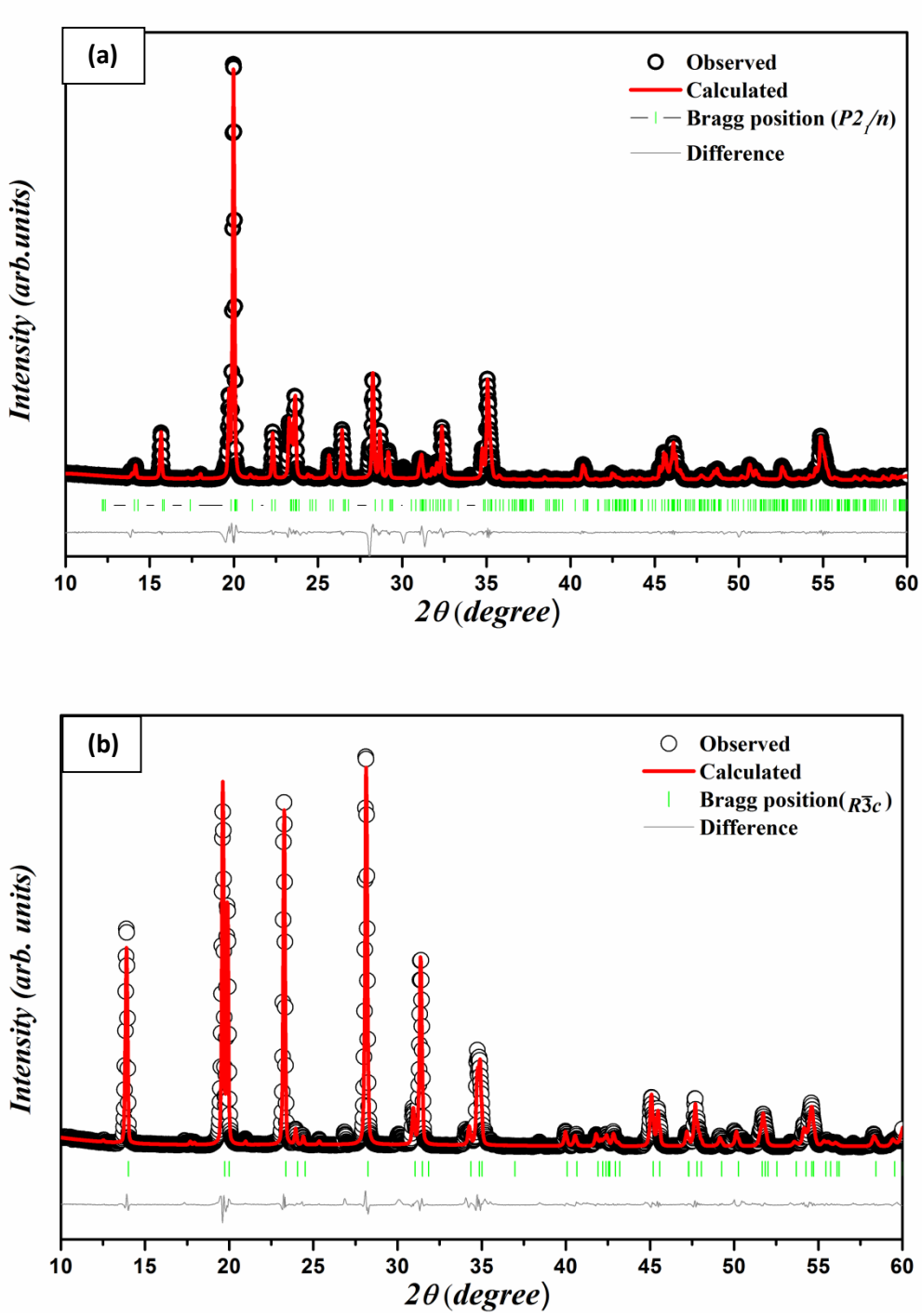

Figure 19: Rietveld refinement of powder XRD patterns for LZP-10-M (a) and LZP-10-R (b). The open circle symbols are observed data points, the solid lines are the refinement result, and bottom lines represent the difference in the observed and calculated plot. The vertical bars are the Bragg positions of the reflections in the space group $P2_1/n$ (a) and $R\bar{3}c$ (b).

Rietveld refinements were carried out using TOPAS 3.0 software. A good fit between the observed and calculated patterns for all samples is evident. The calculated structural parameters for both the phases are provided in Table 5 and Table 6. The volume of the unit cell shows a gradual increase with the increase in the content of $(SiO_4)^{4-}$. This gradual increase of volume can be related to the greater ionic radius of Si when compared to P.

Sample	LZP-00	LZP-05	LZP-10
a (Å)	8.8181(18)	8.8232(81)	8.8373(52)
b (Å)	8.9462(20)	8.9457(77)	8.9473(48)
c (Å)	12.3897(37)	12.3787(11)	12.3966(69)
β (°)	90.4762	90.2975	90.0638
Cell Volume(Å^3)	977.37(78)	977.05(15)	980.21(95)

Table 5: Refined structure parameters for monoclinic phase (cell parameters: a, b, and c; angle β; cell volume.

Sample	LZP-00	LZP-05	LZP-10
a (Å)	8.8340(12)	8.8551(14)	8.8678(39)
b (Å)	8.8340(12)	8.8551(14)	8.8678(39)
c (Å)	22.250(40)	22.2205(37)	22.1765(11)
Cell Volume(Å^3)	1503.79(50)	1508.94(48)	1510.2(15)

Table 6: Refined structure parameters for rhombohedral phase (cell parameters: a, b, and c; cell volume).

4.3 FIELD EFFECT SCANNING ELECTRON MICROSCOPY

FESEM images of the LZP-00-M and LZP-00-R pellets sintered at 900 °C and 1300 °C are shown in Figure 20. For the LZP-00-M sample, average grain size was calculated using Image J software is 550 nm with the standard deviation of 120 nm (Figure 20 (a)). Large inter-granular pores are visible indicating poor sintering of monoclinic phase at 900 °C. With the increase in sintering temperature to 1300 °C, along with the change in crystal structure to a rhombohedral phase, there is also a significant increase in the average grain size. As seen in figure 20

(b), grains with size in a range of ~ 1-20 μm are observed for LZP-00-R. The average grain size is estimated for this sample was ~ 12 μm with the standard deviation of ~ 2 μm. There is a moderate improvement in the relative density of LZP-00-R (~ 80% of theoretical density) as compared to LZP-00-M (~ 76% of theoretical density). Inter-granular micro-cracks can be seen in Figure 20(b). These micro-cracks that result in poor sintering ability are attributed to the anisotropic thermal expansion of NaSICON-type rhombohedral phase along a- and c-axes [78].

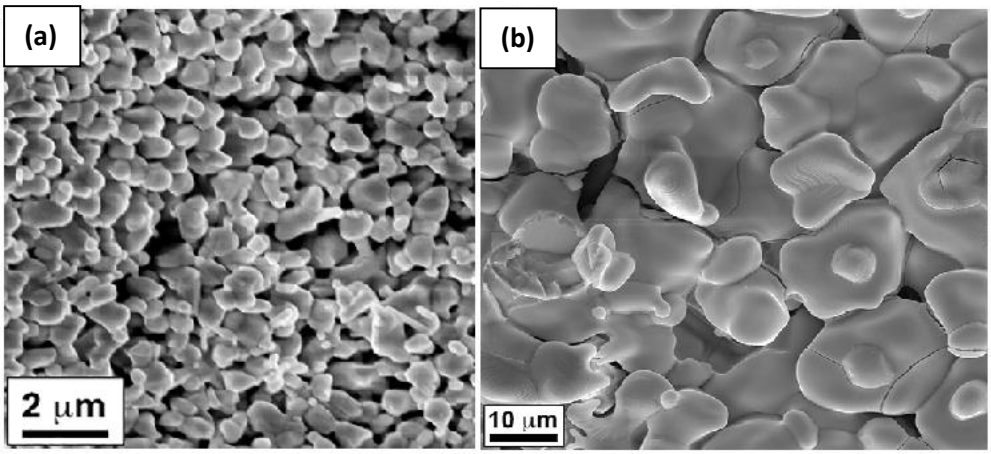

Figure 20: FESEM images of (a) LZP-00-M pellet sintered at 900 °C and (b) LZP-00-R pellet sintered at 1300 °C.

4.4 COMPLEX IMPEDANCE SPECTROSCOPY

4.4.1 Complex Impedance Spectroscopy of pure $LiZr_2(PO_4)_3$ polymorphs.

Complex Impedance Spectroscopy was employed to study the conduction mechanism in pure LZP samples sintered at 900 °C and 1300 °C. Nyquist plots (-Z″ versus Z′) for pure LZP measured at several temperatures are shown in Figure 21 (a), (b), (c) and Figure 22 (a). Nyquist plots appeared as

semicircular arcs with the intercept on Z′-axis on low-frequency side, which eventually decreased with the increase in temperature. A single semicircular arc on the high-frequency side passing almost through the origin is observed in the entire temperature range. A slight deviation in the semicircular arc was observed on the low-frequency side which becomes more prominent with the increase in temperature. This feature could be attributed to the space charge polarization at the grain boundaries and the sample-electrode interface. To estimate the effective bulk resistance, complex impedance data were fitted to an equivalent circuit model of a constant phase element (Q_E), a resistor (R_G), and a capacitor (Q_G) in parallel combination as shown in the Figure 21 (e), 22 (b). Here, Q_E represents the pseudo-capacitor with impedance $Z_Q^* = \{Q_o(j\omega)^n\}^{-1}$. R_G represents the low frequency limiting resistance, and Q_G represents the limiting high-frequency bulk permittivity of the material. This equivalent circuit fits the impedance data reasonably well in the entire temperature range, and a representative fitting of experimental data for different samples at a particular temperature is shown as the solid red line in Figure 21 (d), 22(a).

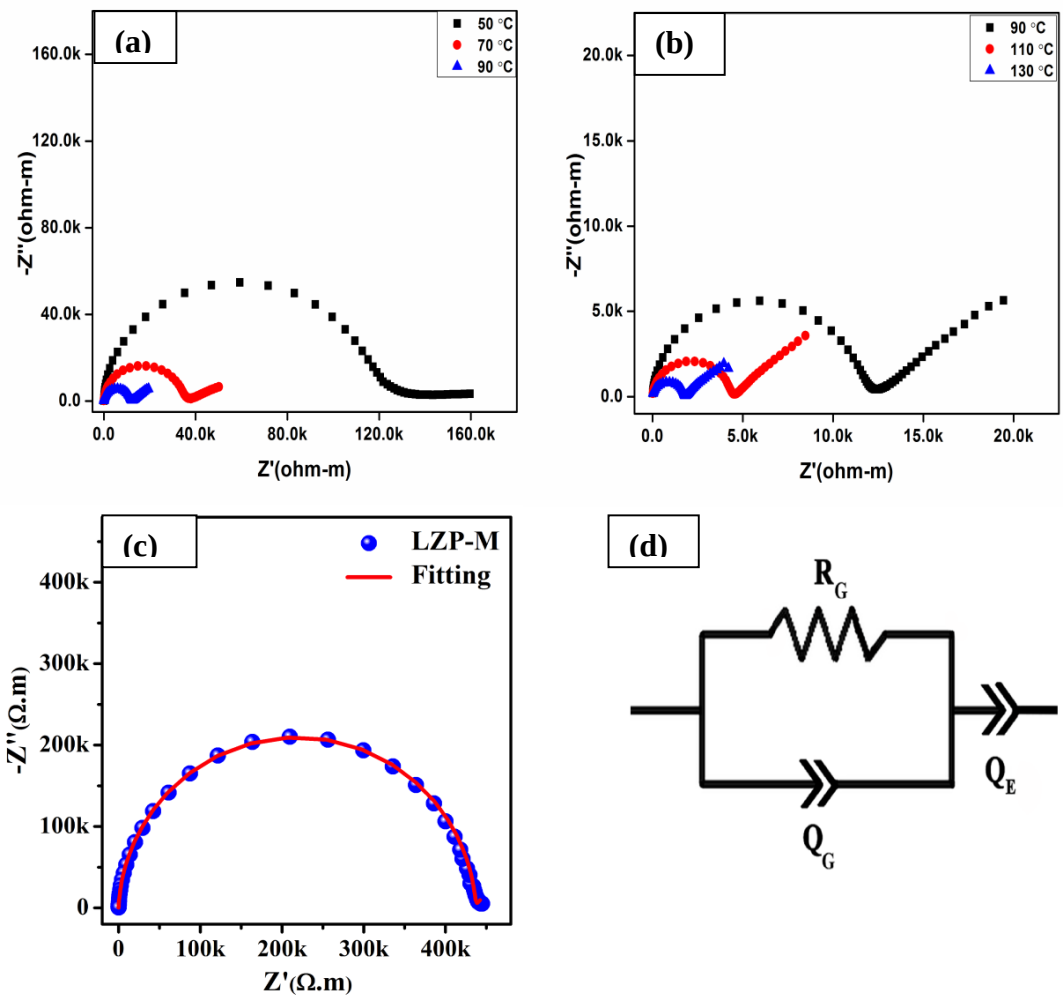

Figure 21:Nyquist plots of $LiZr_2(PO_4)_3$ (pure) sample sintered at 900 °C (a) recorded in temperature range 50 °C to 90 °C, (b) recorded in temperature range 90 °C to 130 °C. (c) Representative measured impedance data (open symbols) and equivalent circuit fitting result (solid red line) at RT (30 °C), (d) schematic diagram of the equivalent circuit used to fit the experimental data.

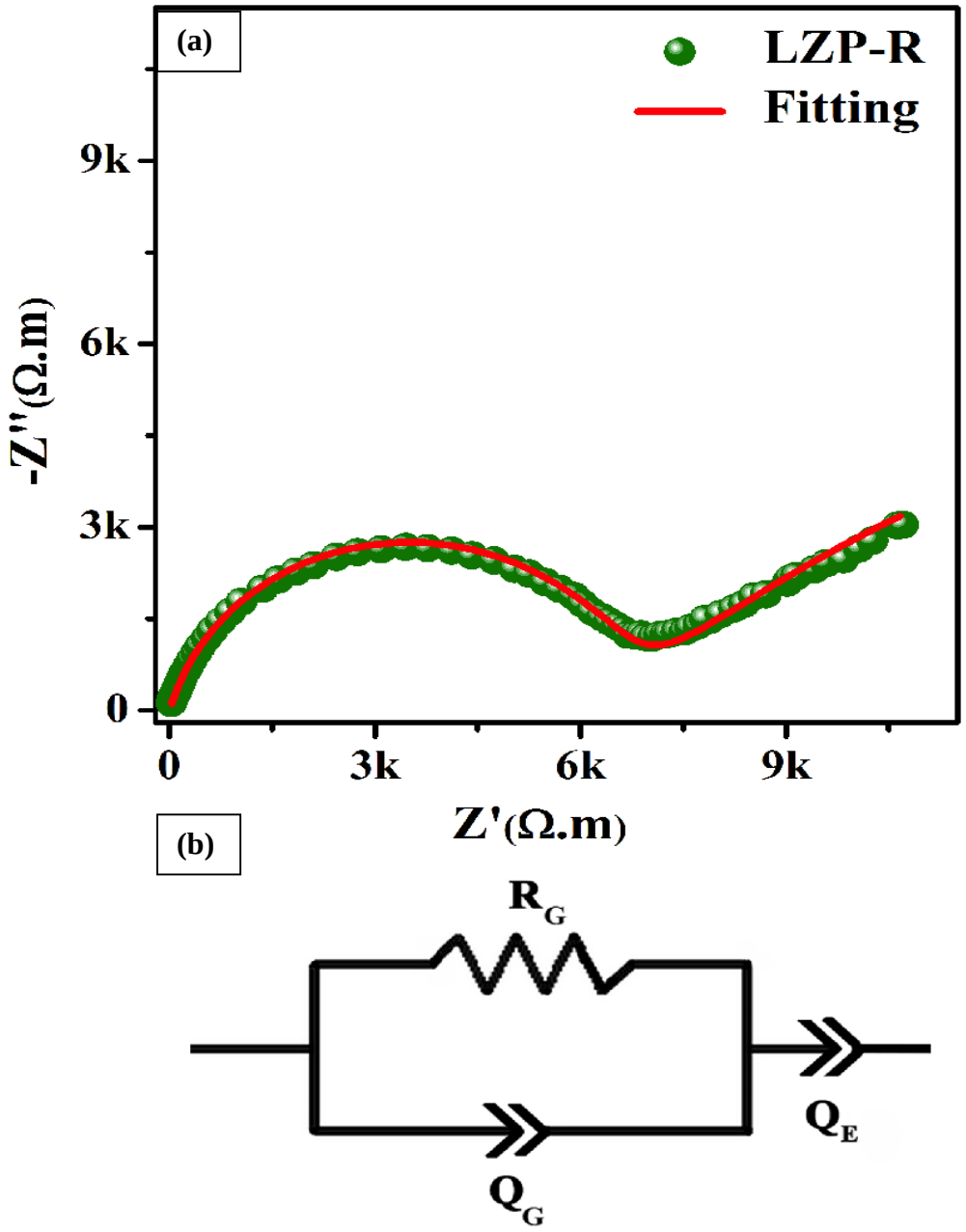

Figure 22: (a) Nyquist plot of LZP-00-R pellet recorded at RT along with the fitting. (30 °C). Scattered symbols are measured data and the solid line is the fitting result. (b) Schematic of the equivalent circuit used for fitting measured data.

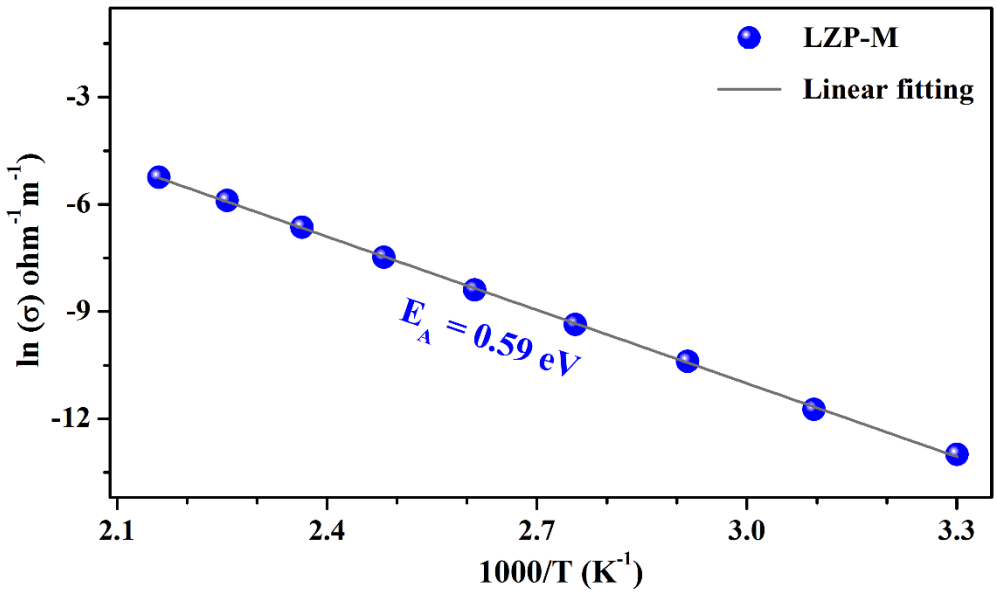

Figure 23: Temperature dependence of the conductivity of LZP-00-M pellet. The solid line is the linear fit to the Arrhenius equation.

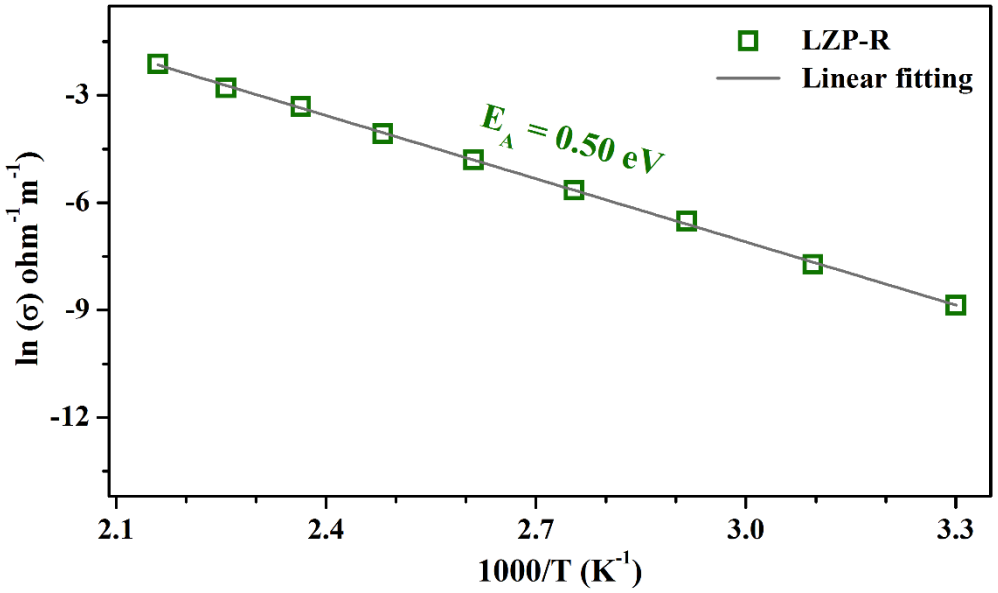

Figure 24: Temperature dependence of the conductivity of LZP-00-R pellet. The solid line is the linear fit to the Arrhenius equation.

Figure 23 and Figure 24 shows the temperature dependence of conductivity ofLZP-00-M and LZP-00-R samples. The solid lines are the linear fit of the

Arrhenius equation. The plot between ln (σ) and 1000/T follows a nearly linear relationship in the studied temperature range and has been fitted according to the Arrhenius equation:

$$\sigma = \sigma_o \exp(-E_A/k_B T) \qquad (10)$$

where σ_o is the pre-exponential factor; E_A is the activation energy per charge carrier; k_B is the Boltzmann's constant; and T is the absolute temperature. The conductivity data follow the Arrhenius law reasonably well in the entire studied temperature range. Table 7 shows the room temperature conductivity and activation energy for the entire studied temperature range for pure LZP samples sintered at 900 °C and 1300 °C. RT conductivity data shows a gradual increase in the conductivity when the crystal structure changes from monoclinic to rhombohedral. Also, the activation energy value differs for above polymorphs. The difference in the activation energy of the samples can be attributed to the change in interfacial resistance at the interface of solid electrolyte samples and silver electrodes.

SAMPLES	LZP-00-M	LZP-00-R
Room temperature conductivity (ohm^{-1} m^{-1})	2.25 X 10^{-6}	1.41 X 10^{-4}
Activation energy (E_A) eV	0.59 ± 0.01	0.50 ± 0.01

Table 7: RT conductivity (σ_{RT}) and activation energy (E_A) in the studied temperature range for pure LZP samples sintered at 900 °C and 1300 °C.

The conductivity value for rhombohedral was found to be two orders higher than that of monoclinic phase with a reduction in activation energy value. Higher conductivity value and lower activation energy value suggest facile lithium conduction in rhombohedral phase as compared to the monoclinic phase. This is due to the presence of unoccupied sites available in the rhombohedral phase that provide three-dimensionally connected pathway for the lithium migration.

4.4.2 Complex Impedance Spectroscopy of Si-doped Monoclinic $LiZr_2(PO_4)_3$ Ceramics..

Nyquist plots (-Z″ versus Z′) for $Li_{(1+3x)}Zr_2(P_{(1-x)}Si_xO_4)_3$ (x= 0.05 and 0.1 sample sintered at 900 °C measured at several temperatures are shown in Figure 25 (a), (b), (c) and Figure 26 (a), (b), (c) . Nyquist plots appeared as semicircular arcs with the intercept on Z′-axis on low-frequency side, which eventually decreased with the increase in temperature. A single semicircular arc on the high-frequency side passing almost through the origin is observed in the entire temperature range. A slight deviation in the semicircular arc was observed on the low-frequency side which becomes more prominent with the increase in temperature. This feature could be attributed to the space charge polarization at the grain boundaries and the sample electrode interface. To estimate the effective bulk resistance, complex impedance data were fitted to an equivalent circuit model of a constant phase element (Q_E), a resistor (R_G), and a capacitor (Q_G) in parallel combination as shown in the Figure 25 (e), 26 (e). The equivalent circuit fits the impedance data reasonably well in the entire temperature range, and a representative fitting of experimental data for different samples at a particular temperature is shown as the solid red line in Figure 25 (d), 26(d).

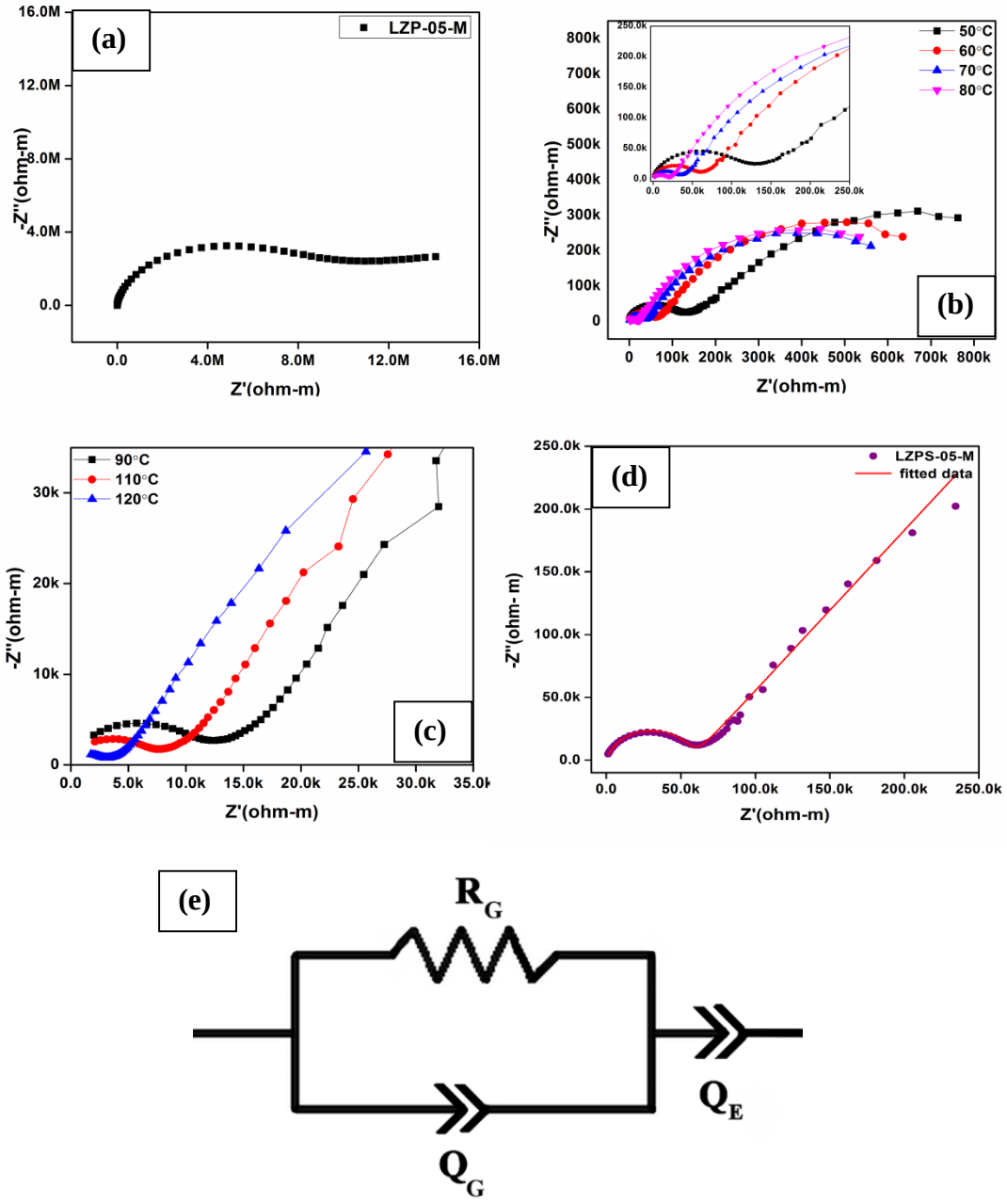

Figure 25: Nyquist plots of $Li_{1.15}Zr_2(P_{0.95}Si_{0.05}O_4)_3$ (5% doped) sample sintered at 900 °C (a) recorded at RT (30 °C), (b) recorded in temperature range 50 °C to 80 °C; inset shows the semicircular arc at different temperatures, (c) recorded in temperature range 90 °C to 120 °C (d) Measured impedance data (open symbols) and equivalent circuit fitting result (solid red line) at 60 °C. (e) Schematic diagram of the equivalent circuit used to fit the experimental data.

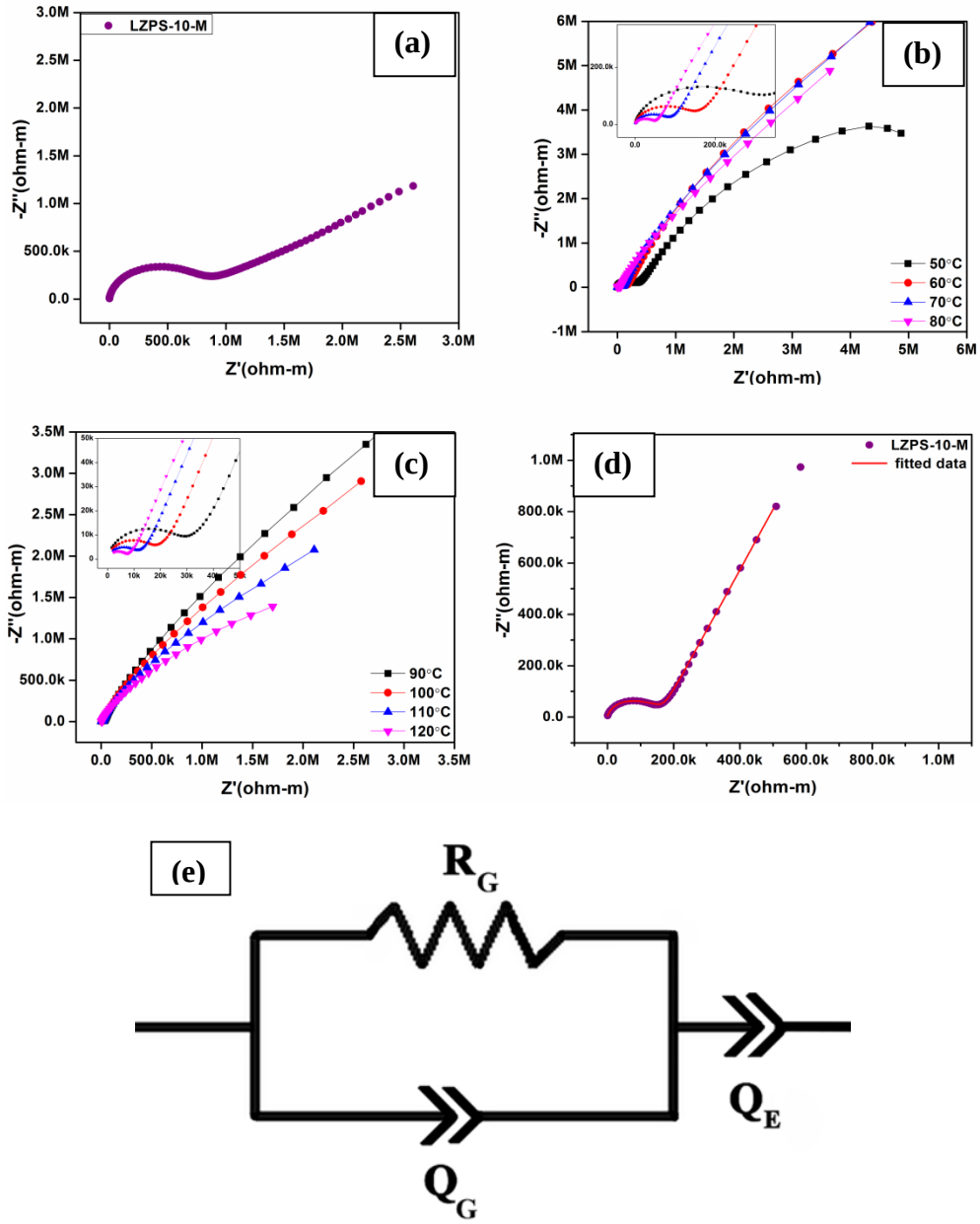

Figure 26: Nyquist plots of $Li_{1.3}Zr_2(P_{0.9}Si_{0.1}O_4)_3$ (10% doped) sample sintered at 900 °C (a) recorded at RT (30 °C), (b) recorded in temperature range 50 °C to 80 °C; inset shows the semicircular arcs at various temperatures, (c) recorded in temperature range 90 °C to 120 °C (d) Measured impedance data (open symbols) and equivalent circuit fitting result (solid red line) at 60 °C. (e) Schematic diagram of the equivalent circuit used to fit the experimental data.

Figure 27 shows the temperature dependence of the conductivity of (a) LZP-05-M and (b) LZP-10-M samples. The solid lines are the linear fit of the Arrhenius equation. The plot between ln (σ) and 1000/T follows a nearly linear relationship in the studied temperature range and has been fitted according to the Arrhenius equation.

The conductivity data follow the Arrhenius law reasonably well in the entire studied temperature range. Table 8 shows the room temperature conductivity and activation energy for the entire studied temperature range for LZPS-05-M and LZPS-10-M sample. Room temperature conductivity data shows a gradual increase in the conductivity with the increase in $(SiO4)^{4-}$ content. Also, the activation energy values differ for the samples. The difference in the activation energy of the samples can be attributed to the change in interfacial resistance at the interface of solid electrolyte samples and silver electrodes.

SAMPLES	LZP-05-M	LZP-10-M
Room temperature conductivity (ohm^{-1} m^{-1})	$9.14*10^{-5}$	$2.64*10^{-4}$
Activation energy (E_A) eV	0.41 ± 0.01	0.52 ± 0.01

Table 8: RT ionic conductivity (σ_{RT}) and activation energy (E_A) for LZPS-05-M and LZPS-10-M sample.

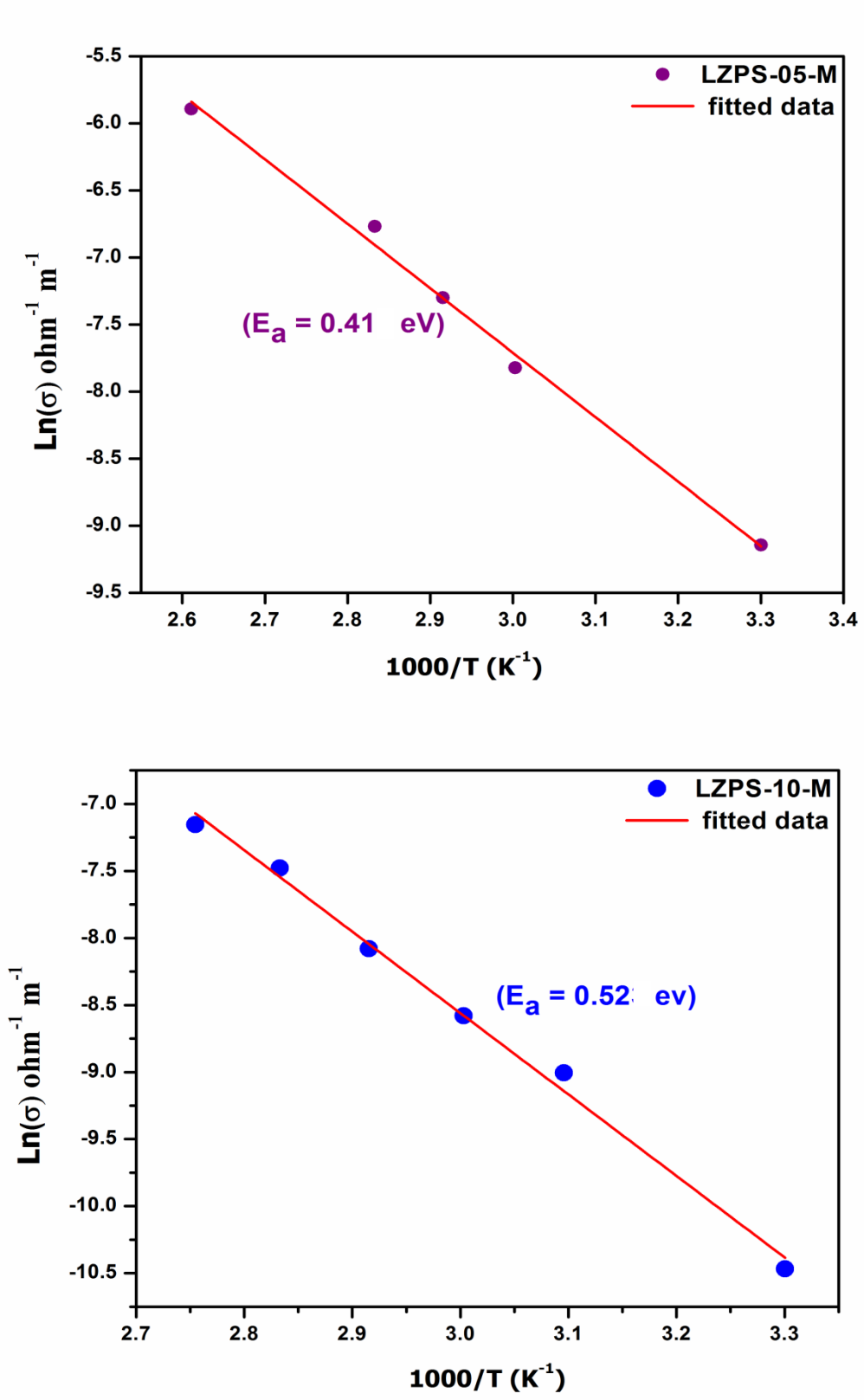

Figure 27: The temperature dependence of conductivities of (a) LZPS-05-M (b) LZPS-10-M pellets. The solid line is linear fit to the Arrhenius equation.

4.4.3 Complex Impedance Spectroscopy of Si-doped Rhombohedral $LiZr_2(PO_4)_3$ Ceramics.

Nyquist plots (-Z″ versus Z′) for $Li_{1.3}Zr_2(P_{0.9}Si_{0.1}O_4)_3$ rhombohedral phase measured at room temperature is shown in Figure 28 (a). Nyquist plots appeared as semicircular arcs with the intercept on Z′-axis on low-frequency side. A single semicircular arc with the high-frequency side passing almost through the origin is observed. Effect of space charge polarization can be easily observed in the lower frequency region. To estimate the effective bulk resistance, complex impedance data were fitted to an equivalent circuit model as shown in the Figure 28 (b). The equivalent circuit fits the impedance data reasonably well and a representative fitting of experimental data for different samples at room temperature is shown as the solid red line in Figure 28 (a).

Figure 29 (a) shows the Nyquist plot for $Li_{1.3}Zr_2(P_{0.9}Si_{0.1}O_4)_3$ (10% doped) sample sintered at 1300 °C measured at RT. A semicircular arc is obtained which is passing almost through origin on the high-frequency side. On the low-frequency side, plot intersects on the x-axis. High-temperature impedance measurements suggest good lithium ion conductivity with the increase in temperature. Figure 29 (b), (c), (d), and (e) show such high-temperature dielectrics of 10 % doped sample. To estimate the effective bulk resistance, complex impedance data were fitted to an equivalent circuit model of a constant phase element (Q_E), a resistor (R_G), and a capacitor (Q_G) in parallel combination as shown in the Figure 29 (f). This equivalent circuit fits the impedance data reasonably well.

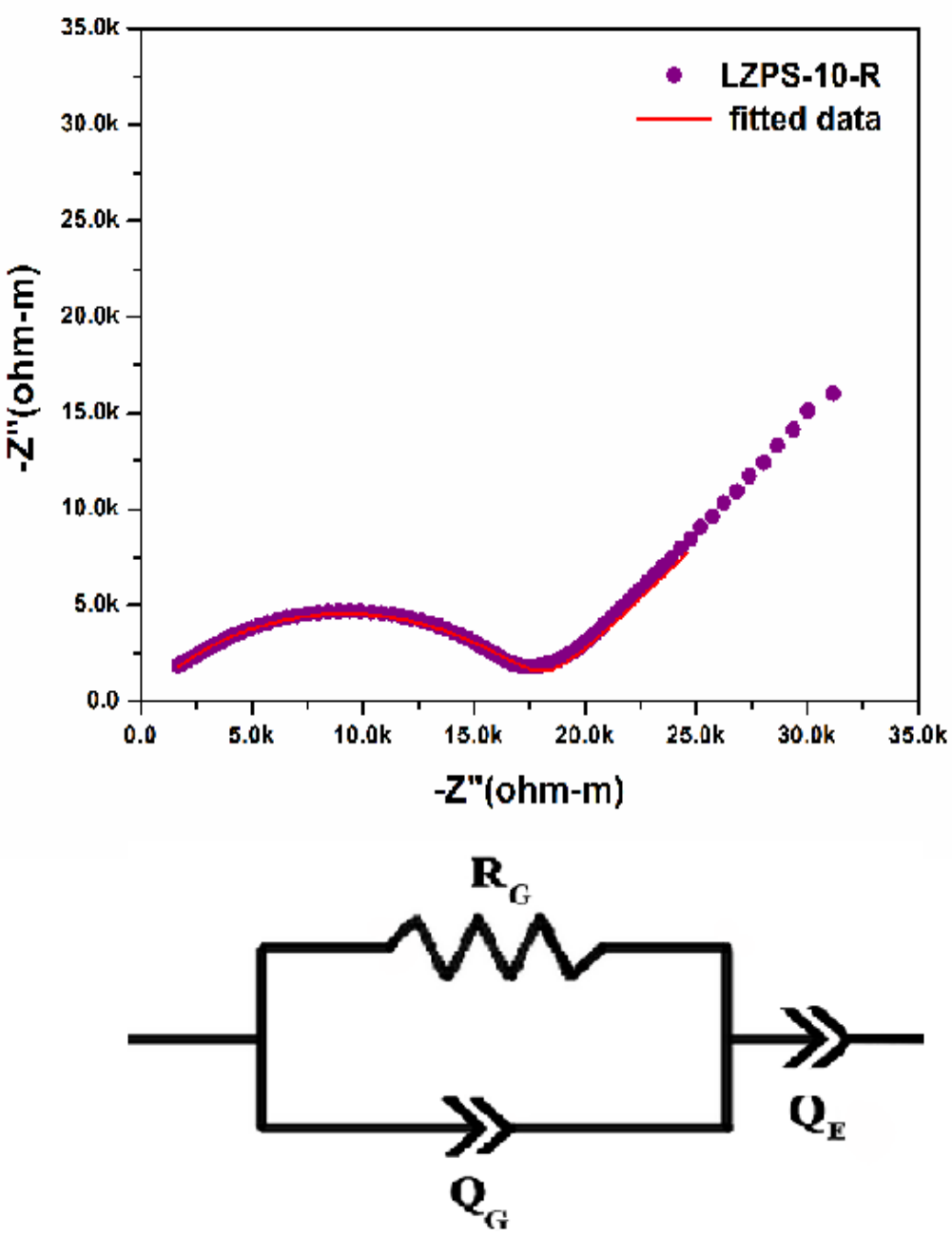

Figure 28: (a) Nyquist plot of LZPS-10-R pellet recorded at RT (30 °C). Scattered symbols are measured data, and the solid line is the fitting result. (b) Schematic of the equivalent circuit used for fitting measured data.

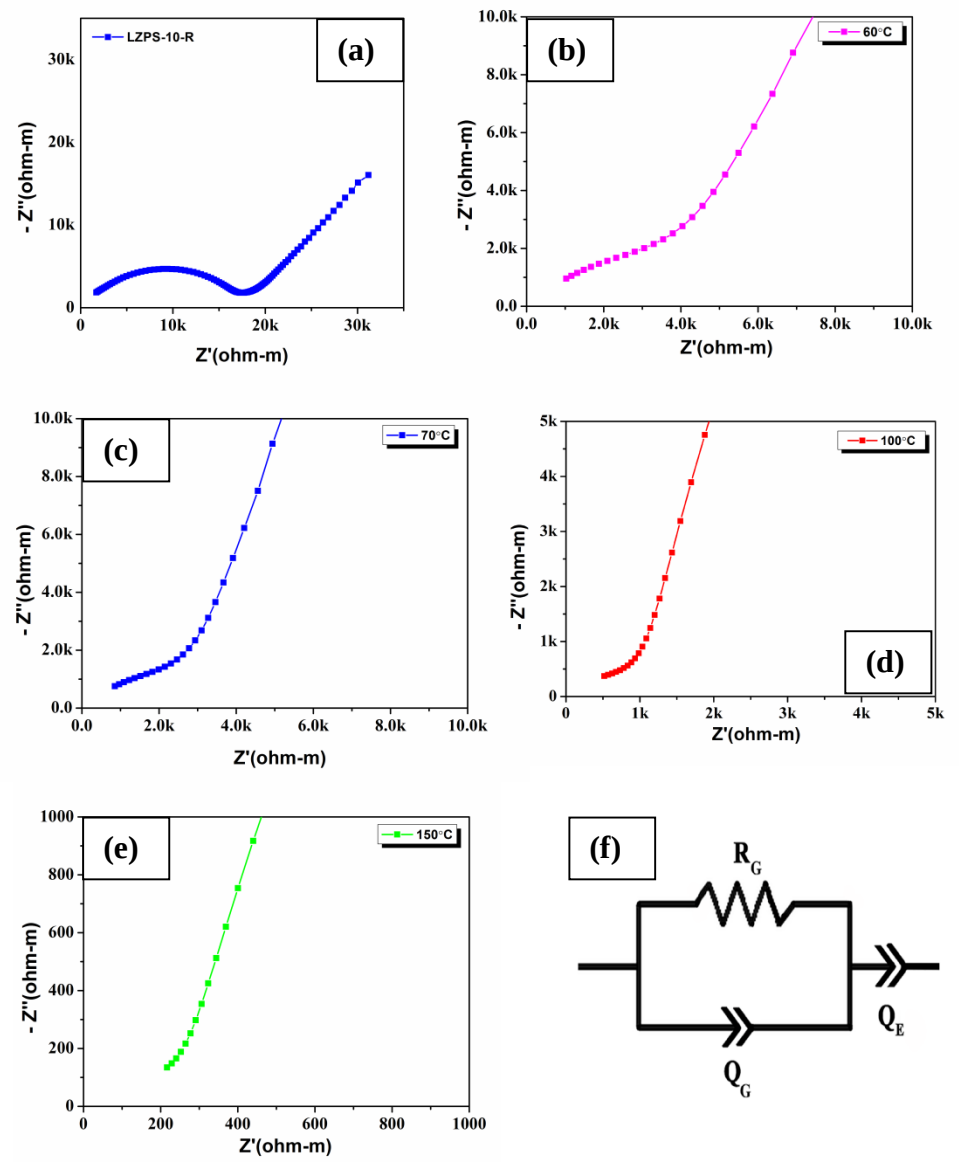

Figure 29: Nyquist plots of LZPS-10-R sample at (a) RT (b) 60 °C (c) 70 °C (d) 100 °C (e) 150 °C. (e) Schematic of the equivalent circuit used to fit the Nyquist plot.

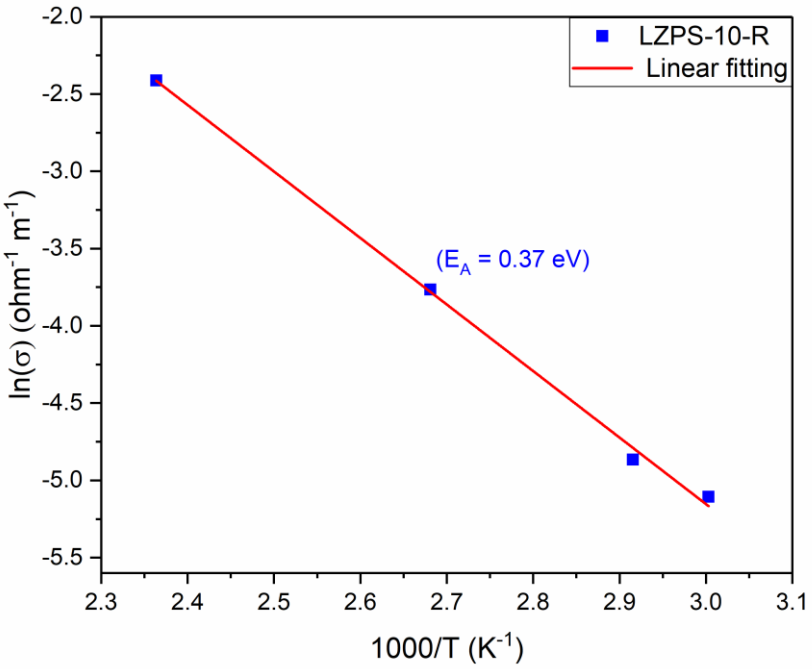

Figure 30: The temperature dependence of the conductivity of LZPS-10-R pellet. The solid line is linear fit to the Arrhenius equation.

Figure 30 shows the temperature dependence of the conductivity of LZPS-10-R sample sintered at 1300 °C. The solid line is the linear fit of the Arrhenius equation. The plot between ln (σ) and 1000/T follows a nearly linear relationship in the studied temperature range and has been fitted according to the Arrhenius equation. The conductivity data follow the Arrhenius law reasonably well in the entire studied temperature range. From the temperature dependence conductivity plot room temperature ionic conductivity of LZPS-10-R sample was found to be 1.61 X 10^{-3} ohm^{-1} m^{-1} with an activation energy of 0.37 ± 0.01 eV. Activation energy shows a significant decrease with the increase in doping concentration which can be attributed to the facile lithium ion transport in doped samples. Room temperature ionic conductivity also shows an improvement from 1.41 X 10^{-4} ohm^{-1} m^{-1} for pure LZP to 1.61 X 10^{-3} ohm^{-1} m^{-1} for x= 0.1 sample.

CHAPTER 5

CONCLUSIONS

In summary, $Li_{1+3x}Zr_2(P_{1-x}Si_xO_4)_3$ (where x = 0, 0.05, and 0.1) powders were synthesized using a modified sol-gel method. Rietveld refinement of room temperature powder XRD data revealed that samples sintered at 900 ºC crystallize in monoclinic phase with $P2_1/n$ space group whereas on increasing the sintering temperature to 1300 ºC, samples adopt rhombohedral structure with space group $R\bar{3}c$.

From the density measurement value, it was obtained that rhombohedral phase of sample $Li_{(1+3x)}Zr_2(P_{(1-x)}Si_xO_4)_3$ (x = 0;0.05 and 0.1) was denser than the monoclinic phase. Also with the increase in the amount of $(SiO_4)^{4-}$ in the sample, density was enhanced greatly.

FE-SEM results also support rhombohedral phase to be denser than monoclinic counterparts.

RT ionic conductivity improved significantly on phase transformation from monoclinic to rhombohedral phase nearly around two orders higher. Temperature dependence of DC conductivities for both the phases was found to follow the Arrhenius equation. Relatively facile lithium-ion conduction in rhombohedral phase was attributed to the improved density and the presence of empty lithium sites that form three-dimensionally connected tunnels for lithium ion migration.

REFERENCES

1. Hu M., *et al.,* (2013), Recent progress in high-voltage lithium ion batteries, Journal of Power Sources. 237, 229-242.
2. Kraytsberg A., *et al.,* (2012), Higher, Stronger, Better… A Review of 5 Volt Cathode Materials for Advanced Lithium-Ion Batteries, Advanced Energy Materials. 2, 922-939.
3. Melot B.C., *et al.,* (2013), Design and Preparation of Materials for Advanced Electrochemical Storage, Accounts of Chemical Research. 46, 1226-1238.
4. Zu C.-X., *et al.,* (2011), Thermodynamic analysis on energy densities of batteries, Energy & Environmental Science. 4, 2614-2624.
5. Brutti S., *et al.,* (2013), Insights about the irreversible capacity of $LiNi_{0.5}Mn_{1.5}O_4$ cathode materials in lithium batteries, Electrochimica Acta. 106, 483-493.
6. Pieczonka N.P.W., *et al.,* (2013), Impact of Lithium Bis(oxalate)borate Electrolyte Additive on the Performance of High-Voltage Spinel/Graphite Li-Ion Batteries, The Journal of Physical Chemistry C. 117, 22603-22612.
7. Verrelli R., *et al.,* (2013), A new, high performance $CuO/LiNi_{0.5}Mn_{1.5}O_4$ lithium-ion battery, Journal of Materials Chemistry A. 1, 15329-15333.
8. Wu X., *et al.,* (2014), Promoting long-term cycling performance of high-voltage Li_2CoPO_4F by the stabilization of electrode/electrolyte interface, Journal of Materials Chemistry A. 2, 1006-1013.
9. Pieczonka N.P.W., *et al.,* (2013), Understanding Transition-Metal Dissolution Behavior in $LiNi_{0.5}Mn_{1.5}O_4$ High-Voltage Spinel for Lithium Ion Batteries, The Journal of Physical Chemistry C. 117, 15947-15957.
10. Sun Y.K., *et al.,* (2002), Synthesis and electrochemical properties of ZnO-coated $LiNi_{0.5}Mn_{1.5}O_4$ spinel as 5 V cathode material for lithium secondary batteries (vol 5, pg A99 2002), Electrochemical and Solid State Letters. 5, L1-L1.
11. Armand M., *et al.,* (2008), Building better batteries, Nature. 451, 652.
12. Hu L., *et al.,* (2013), Fluorinated electrolytes for Li-ion battery: An FEC-based electrolyte for high voltage $LiNi_{0.5}Mn_{1.5}O_4$/graphite couple, Electrochemistry Communications. 35, 76-79.

13. Zhang Z., *et al.,* (2013), Fluorinated electrolytes for 5 V lithium-ion battery chemistry, Energy & Environmental Science. 6, 1806-1810.
14. Ding F., *et al.,* (2013), Dendrite-Free Lithium Deposition via Self-Healing Electrostatic Shield Mechanism, Journal of the American Chemical Society. 135, 4450-4456.
15. Li J., *et al.,* (2013), An Artificial Solid Electrolyte Interphase Enables the Use of a $LiNi_{0.5}Mn_{1.5}O_4$ 5 V Cathode with Conventional Electrolytes, Advanced Energy Materials. 3, 1275-1278.
16. Liu D., *et al.,* (2012), Effect of nano $LiFePO_4$ coating on $LiMn_{1.5}Ni_{0.5}O_4$ 5V cathode for lithium ion batteries, Journal of Power Sources. 204, 127-132.
17. Liu J., *et al.,* (2009), Understanding the Improvement in the Electrochemical Properties of Surface Modified 5 V $LiMn_{1.42}Ni_{0.42}Co_{0.16}O_4$ Spinel Cathodes in Lithium-ion Cells, Chemistry of Materials. 21, 1695-1707.
18. Yang K., *et al.,* (2012), Significant improvement of electrochemical properties of AlF_3-coated $LiNi_{0.5}Co_{0.2}Mn_{0.3}O_2$ cathode materials, Electrochimica Acta. 63, 363-368.
19. Zhao S.-X., *et al.,* (2012), Structure and electrochemical performance of single-crystal $Li_{1.05}Ni_{0.1}Mn_{1.9}O_{3.98}F_{0.02}$ coated by Li–La–Ti–O solid electrolyte, Electrochimica Acta. 65, 7-12.
20. Kamaya N., *et al.,* (2011), A lithium superionic conductor, Nature Materials. 10, 682.
21. Sahu G., *et al.,* (2014), Air-stable, high-conduction solid electrolytes of arsenic-substituted Li_4SnS_4, Energy & Environmental Science. 7, 1053-1058.
22. Rangasamy E., *et al.,* (2014), A high conductivity oxide-sulfide composite lithium superionic conductor, Journal of Materials Chemistry A. 2, 4111-4116.
23. Dudney N.J., (2005), Solid-state thin-film rechargeable batteries, Materials Science and Engineering: B. 116, 245-249.
24. Herbert E.G., *et al.,* (2011), Mechanical characterization of LiPON films using nanoindentation, Thin Solid Films. 520, 413-418.

25. Xu J.-J., *et al.,* (2013), Synthesis of Perovskite-Based Porous $La_{0.75}Sr_{0.25}MnO_3$ Nanotubes as a Highly Efficient Electrocatalyst for Rechargeable Lithium–Oxygen Batteries, Angewandte Chemie International Edition. 52, 3887-3890.
26. Yu X., *et al.,* (1997), A Stable Thin-Film Lithium Electrolyte: Lithium Phosphorus Oxynitride, Journal of The Electrochemical Society. 144, 524-532.
27. Patil A., *et al.,* Issue and challenges facing rechargeable thin film lithium batteries. Vol. 43. 2008. 1913-1942.
28. Takada K., (2013), Progress and prospective of solid-state lithium batteries, Acta Materialia. 61, 759-770.
29. Uemura T., *et al.,* (2013), All-solid secondary batteries with sulfide-based thin film electrolytes, Journal of Power Sources. 240, 510-514.
30. Brazier A., *et al.,* (2008), First Cross-Section Observation of an All Solid-State Lithium-Ion "Nanobattery" by Transmission Electron Microscopy, Chemistry of Materials. 20, 2352-2359.
31. Takada K., *et al.,* (2008), Interfacial modification for high-power solid-state lithium batteries, Solid State Ionics. 179, 1333-1337.
32. Takahashi K., *et al.,* (2013), All-solid-state lithium battery with $LiBH_4$ solid electrolyte, Journal of Power Sources. 226, 61-64.
33. Woo J.H., *et al.,* (2012), Nanoscale Interface Modification of $LiCoO_2$ by Al_2O_3 Atomic Layer Deposition for Solid-State Li Batteries, Journal of The Electrochemical Society. 159, A1120-A1124.
34. Goodenough J.B., *et al.,* (2010), Challenges for Rechargeable Li Batteries, Chemistry of Materials. 22, 587-603.
35. Armand M., *et al.,* (2009), Ionic-liquid materials for the electrochemical challenges of the future, Nature Materials. 8, 621.
36. Sun Y.-K., *et al.,* (2009), High-energy cathode material for long-life and safe lithium batteries, Nature Materials. 8, 320.
37. Chen J., *et al.,* (2013), Graphene Materials for Electrochemical Capacitors, The Journal of Physical Chemistry Letters. 4, 1244-1253.
38. Jiang D.-e., *et al.,* (2013), Microscopic Insights into the Electrochemical Behavior of Nonaqueous Electrolytes in Electric Double-Layer Capacitors, The Journal of Physical Chemistry Letters. 4, 1260-1267.

39. Richey F.W., *et al.*, (2012), In Situ Molecular Level Measurements of Ion Dynamics in an Electrochemical Capacitor, The Journal of Physical Chemistry Letters. 3, 3297-3301.
40. Stramare S., *et al.*, (2003), Lithium Lanthanum Titanates: A Review, Chemistry of Materials. 15, 3974-3990.
41. Thangadurai V., *et al.*, (2006), Recent progress in solid oxide and lithium ion conducting electrolytes research, Ionics. 12, 81-92.
42. Knauth P., (2009), Inorganic solid Li ion conductors: An overview, Solid State Ionics. 180, 911-916.
43. Aguesse F., *et al.*, (2014), Enhancement of the Grain Boundary Conductivity in Ceramic $Li_{0.34}La_{0.55}TiO_3$ Electrolytes in a Moisture-Free Processing Environment, Advanced Materials Interfaces. 1, 1300143.
44. Ma C., *et al.*, (2014), Atomic-scale origin of the large grain-boundary resistance in perovskite Li-ion-conducting solid electrolytes, Energy & Environmental Science. 7, 1638-1642.
45. Hasegawa S., *et al.*, (2009), Study on lithium/air secondary batteries—Stability of NASICON-type lithium ion conducting glass–ceramics with water, Journal of Power Sources. 189, 371-377.
46. Imanishi N., *et al.*, (2008), Lithium anode for lithium-air secondary batteries, Journal of Power Sources. 185, 1392-1397.
47. Hartmann P., *et al.*, (2013), Degradation of NASICON-Type Materials in Contact with Lithium Metal: Formation of Mixed Conducting Interphases (MCI) on Solid Electrolytes, The Journal of Physical Chemistry C. 117, 21064-21074.
48. Kanno R., *et al.*, (2000), Synthesis of a new lithium ionic conductor, thio-LISICON–lithium germanium sulfide system, Solid State Ionics. 130, 97-104.
49. Murayama M., *et al.*, (2002), Synthesis of New Lithium Ionic Conductor Thio-LISICON—Lithium Silicon Sulfides System, Journal of Solid State Chemistry. 168, 140-148.
50. Zhang L., *et al.*, (2013), Effect of lithium borate addition on the physical and electrochemical properties of the lithium ion conductor $Li_{3.4}Si_{0.4}P_{0.6}O_4$, Solid State Ionics. 231, 109-115.

51. Bates J.B., *et al.*, (1992), Electrical properties of amorphous lithium electrolyte thin films, Solid State Ionics. 53-56, 647-654.
52. Li J., *et al.*, (2015), Lithium-Ion Batteries: Solid Electrolyte: the Key for High-Voltage Lithium Batteries (Adv. Energy Mater. 4/2015), Advanced Energy Materials. 5.
53. Ruzmetov D., *et al.*, (2012), Electrolyte Stability Determines Scaling Limits for Solid-State 3D Li Ion Batteries, Nano Letters. 12, 505-511.
54. Thangadurai V., *et al.*, (2004), Crystal Structure Revision and Identification of Li+-Ion Migration Pathways in the Garnet-like $Li_5La_3M_2O_{12}$ (M = Nb, Ta) Oxides, Chemistry of Materials. 16, 2998-3006.
55. Thangadurai V., *et al.*, (2003), Novel Fast Lithium Ion Conduction in Garnet-Type $Li_5La_3M_2O_{12}$ (M = Nb, Ta), Journal of the American Ceramic Society. 86, 437-440.
56. Thangadurai V., *et al.*, (2005), $Li_6ALa_2Nb_2O_{12}$ (A=Ca, Sr, Ba): A New Class of Fast Lithium Ion Conductors with Garnet-Like Structure, Journal of the American Ceramic Society. 88, 411-418.
57. Thangadurai V., *et al.*, (2005), $Li_6ALa_2Ta_2O_{12}$ (A = Sr, Ba): Novel Garnet-Like Oxides for Fast Lithium Ion Conduction, Advanced Functional Materials. 15, 107-112.
58. Murugan R., *et al.*, (2007), Schnelle Lithiumionenleitung in granatartigem $Li_7La_3Zr_2O_{12}$, Angewandte Chemie. 119, 7925-7928.
59. Robertson A.D., *et al.*, (1997), Review of crystalline lithium-ion conductors suitable for high temperature battery applications, Solid State Ionics. 104, 1-11.
60. Roy R., *et al.*, (1982), [NZP], a new radiophase for ceramic nuclear waste forms, Materials Research Bulletin. 17, 585-589.
61. Alamo J., *et al.*, (1984), ULTRALOW-EXPANSION CERAMICS IN THE SYSTEM Na_2O-$ZrO_2P_2O_5$-SiO_2, J. Am. Ceram. Soc. 67.
62. Goodenough J.B., *et al.*, (1976), Fast Na+-ion transport in skeleton structures, Materials Research Bulletin. 11, 203-220.
63. Hong H.Y.P., (1976), Crystal structures and crystal chemistry in the system $Na_{1+x}Zr_2Si_xP_{3-x}O_{12}$, Materials Research Bulletin. 11, 173-182.

64. Aono H., *et al.,* (1993), The Electrical Properties of Ceramic Electrolytes for $LiM_xTi_{2-x}(PO_4)_{3+y}Li_2O$, M = Ge, Sn, Hf, and Zr Systems, Journal of The Electrochemical Society. 140, 1827-1833.

65. Basu B., *et al.,* (1986), Ionic conductivity in the system $Li_{9-4x}Zr_x(PO_4)_3$, Solid State Ionics. 21, 231-238.

66. Casciola M., *et al.,* (1990), Preparation, structural characterization and conductivity of $LiTi_xZr_{2-x}(PO_4)_3$, Solid State Ionics. 37, 281-287.

67. Casciola M., *et al.,* (1988), Preparation, structural characterization and conductivity of $LiZr_2(PO_4)_3$, Solid State Ionics. 26, 229-235.

68. Chavez M.d.L., *et al.,* (1986), COMPOUND FORMATION AND PHASE EQUILIBRIA IN THE SYSTEM Li_2O-ZrO_2-P_2O_5, British ceramic. Transactions and journal. 85, 167-171.

69. Kuwano J., *et al.,* (1994), Ionic conductivity of $LiM_2(PO_4)_3$ (M=Ti, Zr, Hf) and related compositions, Solid State Ionics. 70-71, 332-336.

70. Petit D., *et al.,* (1986), Fast ion transport in $LiZr_2(PO_4)_3$: Structure and conductivity, Materials Research Bulletin. 21, 365-371.

71. Taylor B.E., *et al.,* (1977), New solid ionic conductors, Materials Research Bulletin. 12, 171-181.

72. Aono H., *et al.,* (1992), Electrical Properties and Sinterability for Lithium Germanium Phosphate $Li_{1+x}M_xGe_{2-x}(PO_4)_3$, M=Al, Cr, Ga, Fe, Sc, and in Systems, Bull. Chem. Soc. Jpn. 65, 2200-2204.

73. Li S.c., *et al.,* (1988), Phase relationships and electrical conductivity of $Li_{1+x}Ge_{2-x}Al_xP_3O_{12}$ and $Li_{1+x}Ge_{2-x}Cr_xP_3O_{12}$ systems, Solid State Ionics. 28-30, 1265-1270.

74. Aono H., *et al.,* (1993), Electrical properties and crystal structure of solid electrolyte based on lithium hafnium phosphate $LiHf_2(PO_4)_3$, Solid State Ionics. 62, 309-316.

75. Sudreau F., *et al.,* (1989), Dimorphism, phase transitions, and transport properties in $LiZr_2(PO_4)_3$, Journal of Solid State Chemistry. 83, 78-90.

76. Catti M., *et al.,* (2000), Lithium location in NASICON-type Li+ conductors by neutron diffraction: II. Rhombohedral α-$LiZr_2(PO_4)_3$ at T=423 K, Solid State Ionics. 136-137, 489-494.

77. Catti M., *et al.*, (1999), Lithium location in NASICON-type Li+ conductors by neutron diffraction. I. Triclinic α′-$LiZr_2(PO_4)_3$, Solid State Ionics. 123, 173-180.

78. Iwao Y., *et al.*, (1993), Grain Size-Microcracking Relation for $NaZr_2(PO_4)_3$ Family Ceramics, Journal of the American Ceramic Society. 76, 487-491.

79. Roossbach A., et al., (2018), Structural and transport properties of lithium conducting Nasicon materials, J. Power Sources, 391, 1-9

80. Shinawi H., et al., (2018), NASICON $LiM_2(PO_4)_3$ electrolyte (M = Zr) and electrode (M = Ti) materials for all solid-state Li-ion batteries with high total conductivity and low interfacial resistance, J. Mater. Chem. A,6, 5296-5303.

81. Sonni M., et al., (2018), Elaboration, structural study and validation af a new NASICON-type structure, $Na_{0.72}(Cr_{0.48}Al_{1.52})(Mo_{2.77}Al_{0.23})O_{12}$, Acta Crystallogr. E, 74, 406-409.

82. Boisse B., et al., (2016), Alkaline Excess Strategy to NASICON-Type Compounds towards Higher-Capacity Battery Electrodes, J. Electrochem. Soc., 163, A1469-A1473.